Technische Universität München
Fakultät für Physik

Abschlussarbeit im Bachelorstudiengang Physik

Geant4 Simulation eines auf GEM basierten Detektors

Geant4 simulation of a GEM based detector

Gramos Qerimi

16. September 2015

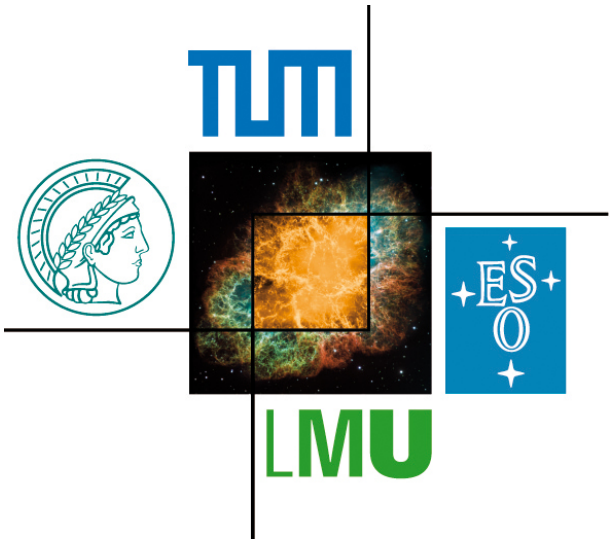

Erstgutachter (Themensteller): Prof. L. Fabbietti
Zweitgutachter: Dr. A. Ulrich

Betreuer: Dr. P. Gasik

Contents

Introduction v

1 Principles of a GEM TPC 1
1.1 Time Projection Chamber 1
1.2 MWPC vs. GEM 3
1.3 GEM stability against electric discharges 7

2 Simulation framework 11
2.1 Detector description in GEANT4 11
2.2 Reference simulations with a point-like source 15
2.3 Simulations with a mixed source 26
2.4 Simulations with additional el. field 36

3 Comparison to the experimental data and outlook 41

A Principal difference between GEM TPC and wire TPC 43

B 2D simulated plots 45

C Time results of the analysis with el. field 47

Bibliography 51

Acknowledgements 53

Introduction

Gated multi-wire proportional chambers (MWPCs), which consist of a grid of wires to amplify and measure signals, are commonly used in a time projection chamber (TPC), the main apparatus of the ALICE experiment located at CERN. This tracking detector with a large gas volume measures the space-time-coordinates of charged particles in high-multiplicity events and is therefore able to reconstruct their trajectories. The TPC operates in gated mode in order to collect the ions produced in the amplification process, that could drift back into the drift volume. Therefore it can prevent possible distortions in reconstructing the tracks (space charge effect). [1]
At the moment in ALICE there are studies of Pb-Pb collisions at a center-of-mass energy of $\sqrt{s} = 2.76$ TeV, and the gating grid is operating with a frequency of 1 kHz. In 2019 however, after the LHC upgrade during the second Long Shutdown, the luminosity and energy of the Pb-nucleons will be increased up to $\sqrt{s} = 5.5$ TeV. That means, that the particle velocities are much higher as before, which corresponds to a collision rate of 50 kHz over the beam time. To fulfill these requirements, the conventional MWPC will be replaced by Gas Electron Multipliers (GEMs). [2]
This new type of the TPC has the capability to reach higher trigger rates so that GEM based detectors would overcome the rate limitations of the gating grid. Therefore the use of Gas Electron Multiplier for gas amplification and intrinsic ion-backflow suppression in the TPC allows a sufficient opportunity to satisfy the major ALICE-TPC upgrade. As a first version, a small detector with three GEM-foils has been built successfully at the Technische Universität München.
During measurements on the stability of this prototype for different HV-settings of the GEMs, there is found a straight correlation between high charge-densities on the foils and sparks. The aim of this bachelor thesis is to study the cause of discharge probabilities on the basis of a detailed GEANT4 simulation in order to explain the condition of this effect, that is responsible for a break-down of the stability and even a harm of the GEM foil.
After showing briefly the technical properties of GEM TPCs and defining the discharge probability, the full simulation framework is introduced in order to describe this relevant effect. The final chapters of the thesis are dedicated to the comparison between the simulation and experimental data followed by a recapitulation between the discharge probability and charge densities in gaseous detectors.

Chapter 1

Principles of a GEM TPC

During decades the development of advanced detector technologies for fast tracking applications has been compelled due to the ever-growing scientific goals in experimental particle physics. Especially the ALICE experiment, which is located in Geneva at CERN, whose main task is to produce and study the quark-gluon-plasma[1], is planning an upgrade in its central barrel, the time projection chamber. [3]

1.1 Time Projection Chamber

A TPC is a technologically advanced detector which has the ability to reconstruct tracks, measure the particle's momentum, determine vertices and identify particles by analyzing the particle's energy loss. The picture below shows the procedure of tracking particles from heavy ion collisions done at the ALICE TPC.

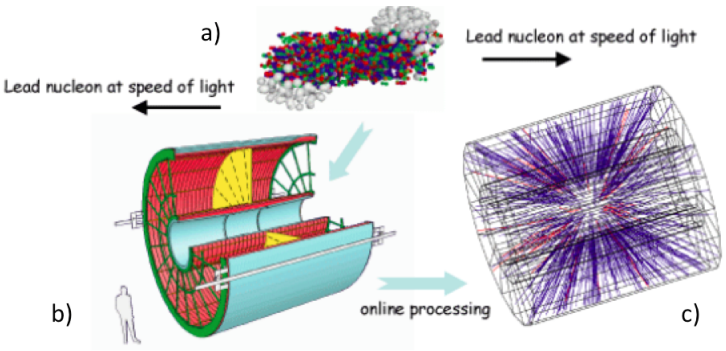

Figure 1.1: Typical process for track reconstruction: a) Collision of Pb-Pb nucleons (colored balls may conform with the quark-gluon-plasma) b) Sketch of the TPC of the ALICE experiment c) An online 3D analysis showing all tracks coming from the vertex of the collision. [4]

[1] A new state of matter predicted by theoretical considerations to explain the physical status immediately after the Big Bang.

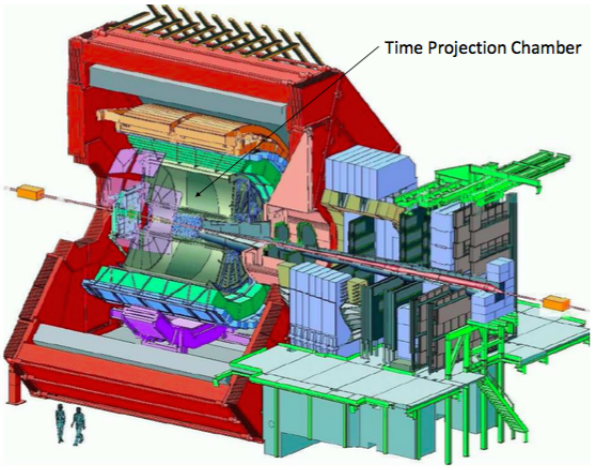

Figure 1.2: Artistic view of the ALICE detector with the TPC in its center. [5]

In fig. 1.2 the size and basic construction of the ALICE detector with the TPC is illustrated. It consists of a large cylindrical volume centered around the interaction vertex, which is inside of a solenoid magnetic field and filled with gas. Therefore almost 4π of the solid angle is covered for minimal information loss. [6]
The active volume of the ALICE TPC is 88 m^3 and the cylinder inside spans 500 cm along the beam axis and extends from 85 cm to 250 cm in radial direction. [7]
Despite its large dimensions (see fig. 1.1 b) and fig. 1.2), the detector reaches a spatial resolution of 300 μm and a dE/dx resolution of 5-7 %. [8]
The concept of reconstructing the tracks runs as follows:
If a charged particle flies through the detection volume, the gas inside the chamber will be ionized. In order to separate the positive gas ions and the released electrons, a homogenous electrical field is applied parallel to the magnetic field. The primary electrons are then amplified and drift towards the anode where they finally can be detected at the readout pads. [9] Out of this the x and y axis can be determined. The next step is to find out the third component of the particle track. This is possible by measuring the drift time as well as knowing all informations about the drift velocity of the electrons for each gas content and drift field.
However the spatial coordinates can be extracted with high precision only if the electric field is highly homogenous. This can be achieved by applying a field cage consisting of a series of conductive strips, which surround the cylindrical volume. Its purpose is to divide the potential from the anode stepwise down to the cathode in order to minimize possible distortions of the drift field. [10]
Also mentionable is the fact that a parallel magnetic field is added that bends the

particle tracks to enable measurements of their momenta. It leads to the additional effect of suppressing the transversal diffusion of the drifting electrons. To sum up, these requirements to the TPC allow not only a 3D reconstruction of the spatial information of the particles but also a good momentum determination. Together with a $\mathrm{d}E/\mathrm{d}x$ measurement the full particle identification can be reached in a TPC.

1.2 MWPC vs. GEM

As already mentioned in the previous section, an electric field in the vessel is needed to separate the electrons from the positive charged ions that were created by a particle traversing the gas volume. Then the positive ions drift towards the central cathode where they are collected, while the negative charged particles travel in opposite direction to the readout anode. Since the primary electrons would induce only a small signal at the readout pads, they have to be multiplied in order to amplify the signal. In a current design of the ALICE TPC the amplification is achieved by taking usage of so called Multiwire Proportional Chambers, MWPCs. Invented in 1968 and developed by Georges Charpak at CERN [11], they consist of three different wire planes: the gating grid, the cathode plane (so called *Frisch grid*) and the amplification (anode) plane. The wires lie in large numbers side by side and parallel to each other to form a grid, and are sufficiently thin ($\sim$ 10 μm) to generate a high electric field ($\sim$ 200 kV/cm) that surrounds them (see fig. 1.3 a)) [12]. The purpose of the Frisch grid is to close up and separate the homogenous drift field from the inhomogeneous field of the amplification wires (see fig. 1.3 b)) [13].

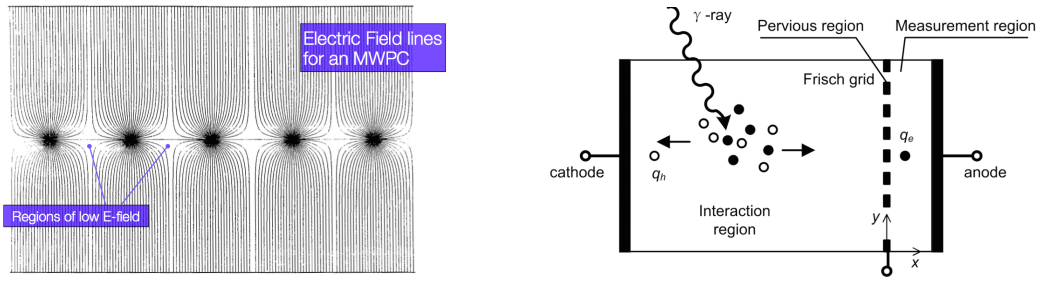

Figure 1.3: a) Left: Illustration of the electric field lines for MWPC. A low field exists only between the wires, b) Right: Schematic of a simple detector with a Frisch grid that divides the gas volume in three regions.

Thus the primary electrons are accelerated so far that they can induce secondary electrons by ionizing again the gas. These electrons are also affected by the field so that they ionize the gas once more. The consequence of this iterating procedure

is a chain reaction followed by an avalanche of electrons, all collected by the wires. Meanwhile the positive ions drift towards the Frisch grid and as a result their induced image charges are registered by the readout pads. [14]
An "Ion Back Flow", i.e. when the ions fly back to the drift volume, could destroy the homogeneity of the electric field. To overcome this relevant problem, MWPC-based TPCs normally use a gating mechanism, i.e. the gating grid placed in front of the amplification stage to collect the positive ions (that indeed could accumulate and induce a space charge effect in the drift volume). The time to switch it on and off is limited to the collection time of the ions, which corresponds to a maximum rate of ca. 1 kHz. Thus using a gating grid causes a dead time in the TPC. [15]

The invention of MWPCs revolutionized the field of gaseous detectors. With a modest accuracy and rate capability, the Multi Wire Proportional Chamber allowed large areas to be instrumented with fast tracking detectors and gives the possibility to localize particle trajectories with sub-mm precision. That's why this kind of drift chamber is a benchmark for the ALICE TPC, designed to cope with extreme instantaneous particle densities produced in heavy ion collisions at the LHC. However, position-sensitive detectors based on wire structures have reached limitations in rate capacity and detector granularity of about 100 μm due to diffusion processes and space charge effects in the gas. [16]
Despite various improvements of MWPCs, the previously mentioned problems together with the practical difficulty to manufacture detectors with a large number of closely lying wires, has motivated the evolution of a new generation of gaseous detectors for high luminosity accelerator science, the Micro-Pattern Gas Detectors (MPGD).[2], which can be classified in two large groups: micromesh-based detectors and hole-type structures. While Micromegas, "Bulk" Micromegas, "Microbulk" Micromegas and "InGrid" instruments belong to the micromesh-based structures, the GEMs, THGEM, RETGEM and MHSP elements take a huge part in the latter group. [16]
In the following chapters GEMs (Gas Electron Multipliers) will be discussed more in detail since the ALICE TPC is going to remove the currently used MWPCs and insert Gas Electron Multipliers during the second long shutdown (LS2) in 2018.[3] [2]

The Gas Electrons Multiplier (GEM), invented by F. Sauli at CERN in 1996,

[2] Actually, before the MPGDs were invented, the Micro-Strip Gas Chamber (MSGC) was developed to solve the difficulties that MWPCs had. However, detailed studies of long-term behavior at high rates have revealed the problem of aging, i.e. a slow degradation of the detector's efficiency due to sustained irradiation, and sensitivity regarding discharges in presence of highly ionizing particles that could damage the whole chamber. [17]

[3] Worth to mention is the fact that GEM-based detectors have already been employed successfully for example at the COMPASS experiment at the SPS at CERN. [18]

consists of a polyimide foil ($\sim$ 50 μm thin) that is copper clad on both sides (each $\sim$ 5 μm thin) and contains a large number of small holes extending through the foil. [19]
The first time developed on the basis of modern photo-lithographic technology and etching mechanism at CERN, GEM holes have a remarkable double conical shape with an inner diameter of only 50-60 μm and outer diameter of 70 μm so that GEM foils form a dense, regular pattern of holes. In a standard configuration, two neighboring holes have a distance of $\sim$ 140 μm from each other.
The mechanism of the electron amplification in GEMs to induce a sufficient signal works as follows: The metal layers play the role of electrodes, and when a high voltage is applied across the copper-insulator-copper structure, a large electric field arises inside the holes. Once released by the primary ionization particle in the upper conversion region above the foil, the electrons pass through the GEM holes where the strong field acting on them induces the cascade. [20]
Fig. 1.4 illustrates a rough draft of the electric field lines and the affected electrons together with the ions, while the dimensions of the GEM structure are showed in fig. 1.5.

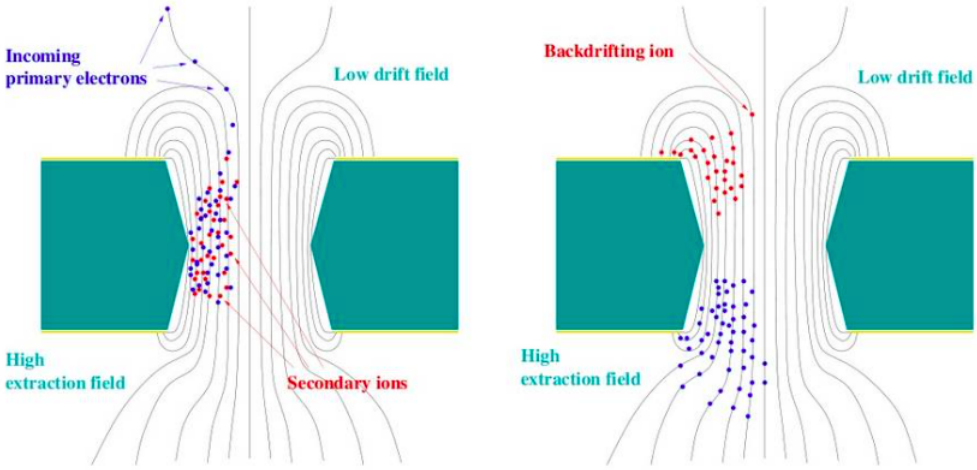

Figure 1.4: Sketch of the cross section of a GEM foil with electric field lines due to the strong potential difference of 300 - 400 V: a) Left: electrons drift into a hole and trigger an avalanche, b) Right: while the electrons drift to the anode, almost all produced ions get collected. [6]

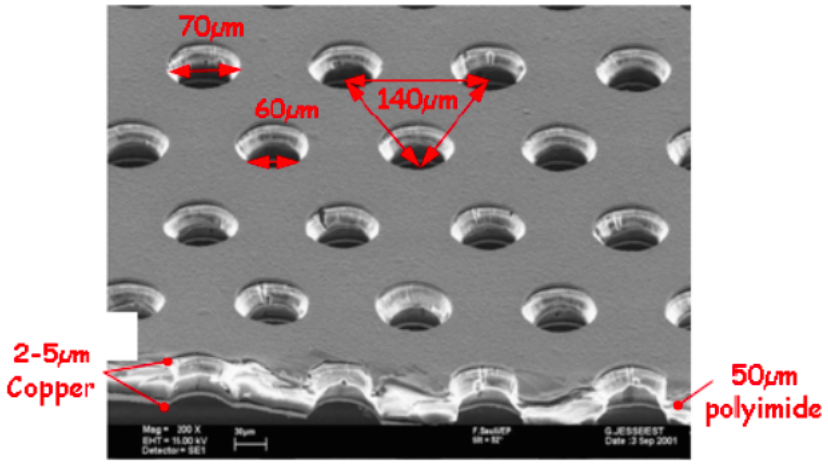

Figure 1.5: Close up view of a GEM foil under an electron microscope with the typical dimensions [6]

Below the GEM holes the electron avalanche can either be extracted or passed to the next amplification stage, i.e. in a multiple GEM-stack (for an example of a GEM based detector with triple GEM foils see fig. 1.6).
Multi-layer GEM detectors are able to reach a gain[4] up to 10^5. [21] At the same time the produced ions drift in opposite direction, but will stack at the upper side of the GEM foil due to the geometrical shape of the holes (the asymmetric field can help reducing the number of backdrifting ions too, see fig. 1.3) and thus are not able to get to the drift volume. Because of that positive effect it follows that the Ion Back Flow is considerably suppressed.
But if the intrinsic suppression is not enough, applying more GEMs into the TPC can solve the problem; e.g. a third GEM above the other two with a configuration that is ideal for ion absorption.

It is clearly evident, that gaseous detectors with multiple GEM foils are very recommended precisely because of both high gain rate and strong Ion Back Flow suppression.

[4] Multiplicity factor of the number of primary electrons

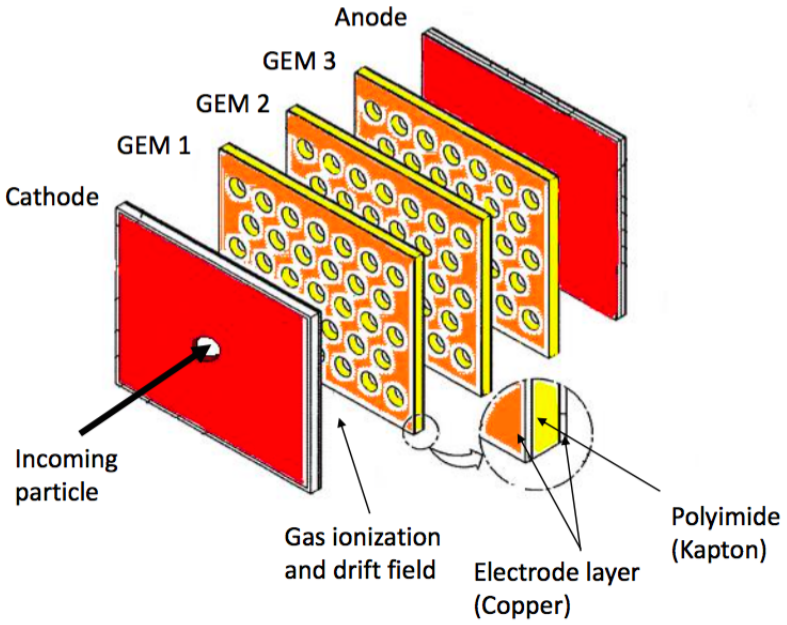

Figure 1.6: Schematic sketch of a gaseous detector with triple GEM design. Behind the latest GEM foil the anode (typically a PCB material covered on one side with a thin copper layer) is mounted to readout the incoming electrons. [22]

A unique property of a detector based on GEMs is the ability to decouple completely the amplification stage (GEM) from the readout electrode (PCB), which operates at unity gain and serves only as a charge collector. The signal can then be created by charge induction on the PCB, without a slow ion tail.
GEM detectors do not only satisfy a wide range of experimental requirements like fast tracking of minimum ionizing particles, good electron collection with small distortions and strong ion feedback suppression, but also have an improved multi-track resolution. In appendix A the fig. A.1 illustrates the difference between GEM and conventional MWPC due to the signal distribution very well.

1.3 GEM stability against electric discharges

Recapitulating, MPGDs (and in particular the GEMs) play an important role in modern physics experiments. Besides their excellent spatial resolution, their fast ion collection allows them to cope with high particle rates. As introduced in section

1.2, the Ion Back Flow[5] is a commonly used quantity to describe the suppression of back drifting ions. Mounting a triple GEM-stack into the TPC can reduce it below one percent. [23]
At very high fluxes, however, the modern GEM detector suffers from a major problem in terms of its stability: the so called electrical discharges (sparks).
A high ionizing particle (e.g. α - particle), that traverses the drift volume, deposits a large amount of its energy by ionizing the gas and thus releasing a lot of electrons and positively charged ions. In other words, it creates a high charge density at a certain point. Then the density will be increased in order to reach a high gain. Now assuming a spark is induced by a local, large charge density, the spark rate grows as a power law with the gain (or number of the electrons) of the detector.
If the certain limit Q_{crit}[6] for electron amplification, the *Raether Limit* [25], is reached or even exceeded, then discharges are very likely to occur. In that case a transition to a streamer mode occurs, leading to a breakdown in the amplification region. The resulting drop of the detector's gain therefore yields detection inefficiency. It can even damage the detector itself. [26]

To quantify systematically the origin and the development of a discharge, extensive experimental studies have been performed to measure the spark rate. In the following chapters discharge probability studies are referred to the experimental data[7] (see fig. 1.7) taken from the Technical Design Report (TDR) of the ALICE collaboration [27].
For that experiment a small-size prototype detector with a triple GEM stack was constructed. The detector was filled with Ne-CO_2-N_2 as well as with Ar-CO_2 (the reason for this gas choice is explained in section 2.1). A mixed nuclide alpha source was placed on top of the cathode, so that during the measurement alphas were send perpendicular to the GEM foils.
In comparison to previous measurements with ^{220}Rn, the resulting difference suggests that the primary charge density arriving at the GEM holes after drift may be too low (due to the track inclination and the diffusion) to affect the stability of the detector. Thus, the measurements were continued with the alpha source. [27]

[5] Generally defined as the ratio of the number of ions arriving at the cathode to the number of electrons arriving at the anode.
[6] The critical total charge in the avalanche is in the order of $Q_{crit} \sim 10^6$ — 10^7 electrons [24]
[7] The experimental data shown in this bachelor thesis represent the current results of recent R&D ("research and development") efforts.

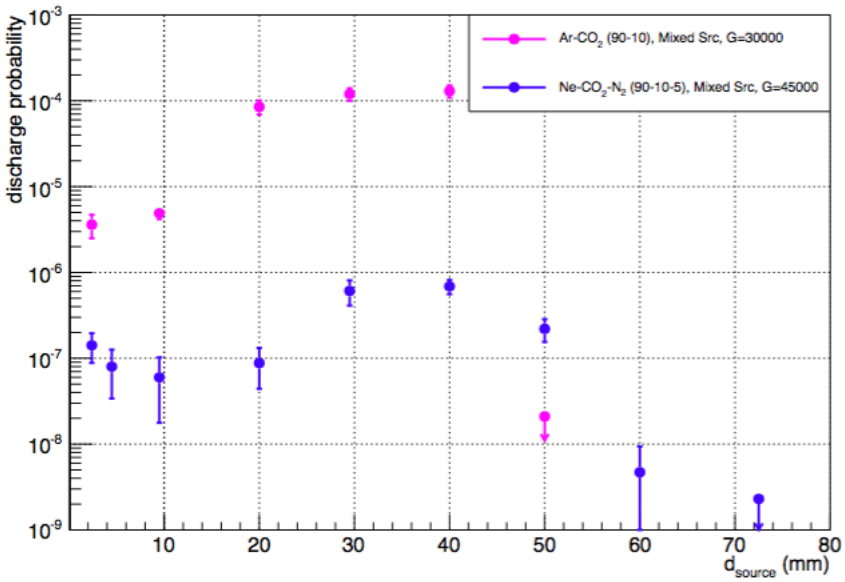

Figure 1.7: Discharge probability as a function of the distance between the alpha source and the GEM stack. Both experimental curves, magenta for Ar-CO_2 and blue for Ne-CO_2-N_2, are performed with a mixed nuclide alpha source (described in section 2.1). Upper limits for the discharge probability for a given distance are indicated with arrows.

The broad plateau in the diagram above indicates that the discharge probability is higher when the alphas penetrate the GEM foils, or even get stopped there. In that case, the highest local primary charge densities in a single GEM hole can be reached. At a certain track length, when the alphas do no longer reach the GEM structure, the probability for inducing a spark drops significantly. It therefore implies that electric discharges depend strongly on the charge density above the GEM holes.

In the next chapter an entire simulation framework of a GEM based gaseous detector is described in order to verify this charge density hypothesis. Afterwards (chapter 3) the results of the simulation will be compared with the experimental data to get a deeper understanding of the discharge phenomena.
Since the intrinsic stability against electric discharges in double or triple GEM stacks is also influenced by other effects, like transfer fields or charge sharing and spreading between the foils, the simulated detector will be implemented with only one single GEM foil to be not biased by these effects.

Chapter 2

Simulation framework

The Gas Electron Multiplier was introduced as a suitable candidate for the upcoming ALICE TPC upgrade. Its physical principles and optical properties were explicitly described in chapter 1. Also the advantages with reference to the conventional MWPCs are discussed in detail, which are generally well understood nowadays. But there is still one hitch, which has a negative impact on the GEMs, namely the electrical discharges. Experimentally observed with a small detector prototype including three GEM foils (see fig. 1.7), the next step is to analyze it in such a way that its cause can physically be explained.
The following sections are dedicated to a GEANT4[1] - based Monte Carlo simulation[2] which describes the geometry and tracking of a virtual detector including the gas, source and the physical processes (e.g. electromagnetic interactions etc.).

2.1 Detector description in GEANT4

The simplest Geant simulation needs three classes and a main program. Besides the physics list[3] and the primary generator action[4], the geometry of the detector has to be classified in the simulation world. [28]
To come as close as possible to the commonly used R&D setup, the detector is implemented with the standard geometry (like the small prototype detector already mentioned in section 1.3). It means, that the detector is composed of a top plate, a gas volume and a readout area. The top plate consists of PCB material and has a thickness of 1.5 mm, the gas volume is 100 mm thick and the readout area is 0.5 mm thick. The height and width remain the same for all components, namely 10 cm x 10 cm. A visualization of the detector is shown in fig. 2.1.

[1] **Ge**ometry **an**d **T**racking: A software package that came out of a research and development study at CERN in 1993 [28]
[2] A Monte Carlo simulation is a statistical method to solve complex problems which aren't analytically solvable. [28]
[3] A class where the physical processes like multiple scattering (G4hMultipleScattering) or ionization of the gas (G4ionIonisation) are implemented.
[4] A class where the events (e.g. α-particles), that are emitted from a source, are defined.

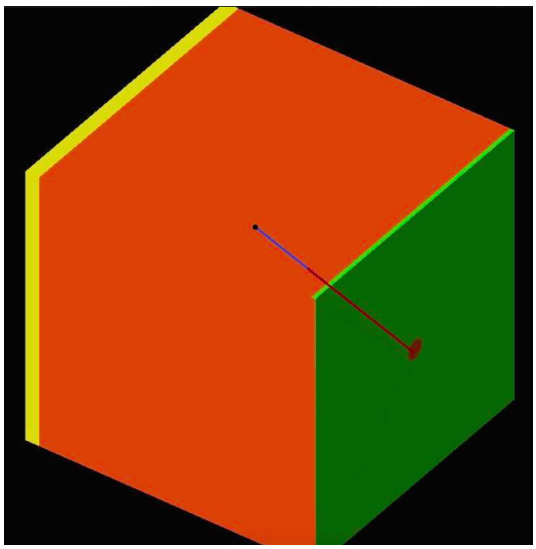

Figure 2.1: Detector setup for the simulations: gas volume (orange) between the readout area (yellow) and the PCB plate (green). The mixed source, placed in the transfixion of the PCB plate, emits alpha particles (dark red), which in turn produce electrons (blue) in the gas volume. The α-particles drift in the volume until they deposit their whole energy in the gas (black point).

In the center of the PCB[5] plate a hole with 7 mm diameter was drilled through, so that the mixed alpha source with same size as the hole can be placed right there.
Before proceeding with the GEANT4 simulation, further informations about the source and the gas content are necessary in order to understand the interaction between the incoming α-particles and the gas molecules.

Informations about the alpha emitters (mixed source):
In the experimental setup, an alpha emitting source (see fig. 2.2) was used. The same radiation source has to be implemented in the simulation. It consists of radionuclides ^{239}Pu, ^{241}Am and ^{244}Cm which are deposited onto a stainless steel disc (25 mm in diameter and 0.5 mm thick). Each component emits ^{4}He - nucleons with an activity of 1 kBq, and the respective energies and intensities are listed in a table on the next page.

[5] PCBs (Printed Circuit Boards) are commonly used, because they are composed of a material called FR4 (flame retardant #4). As the name suggests, FR4 is an industry standard material used in most applications where the spread of fire in electronics is not desired. It has a density of 1.850 g/cm^3. [29]

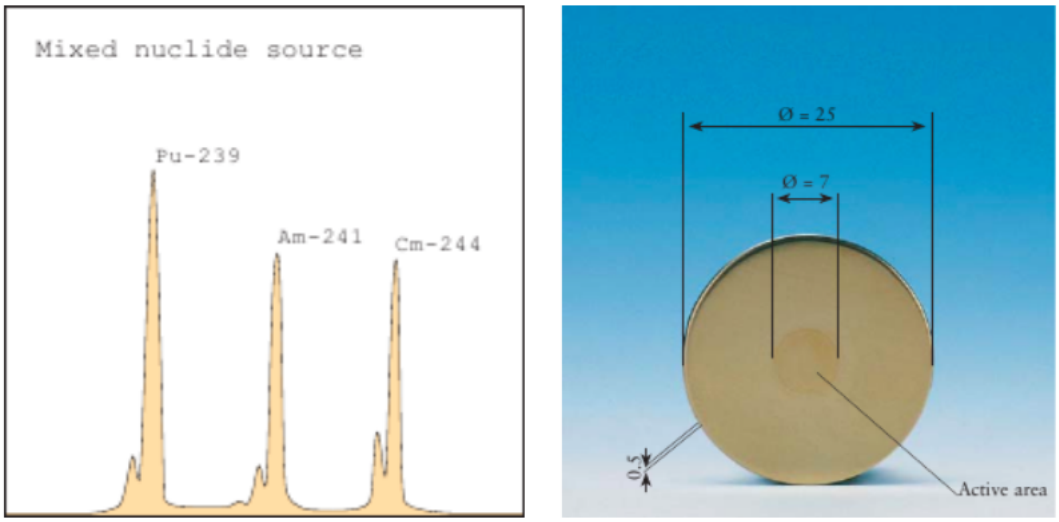

Figure 2.2: Left: Plot of the alpha spectrum. The peaks correspond to the distinct α energies. Right: Dimensions of the mixed source. The radionuclides are placed in the inner disc (7 mm diameter) [30]

Radionuclide	Alpha particle energy [MeV]	Intensity [%]
Pu-239	5.105	11.5
	5.143	15.1
	5.155	73.4
Am-241	5.388	1.4
	5.443	12.8
	5.486	85.2
Cm-244	5.763	23.3
	5.805	76.7

Table 2.1: Each radionuclide of the mixed source emits α-particles with discrete energies and different intensities. [30]

For simplicity in the simulation only the inner disc of the mixed source is implemented without any thickness. Also the solid angle of the radiation is defined in such a way, that the alphas are only emitted into the gas volume. Logically alphas radiated outside of the simulated detector (physical world set in vacuum) play no role in the analysis considered here.

Informations about the gas mixture:
Usually in a TPC the inserted gas consists of two gas components. The one gas component is a noble gas (in the R&D setup, see fig. 1,7, Argon and Neon are used), while the other constituent (so called quencher) is required for stability in the amplification stage. A noble gas has the positive aspect that the atom shells are completely filled with electrons so that it is chemically non-reactive to other gas molecules. Hence it is stable under the standard conditions (300 K, 1 bar atmospheric pressure) the detector is experimentally used and simulated.
During the amplification process some gas atoms can be excited. When they fall down to their ground states, they emit photons in the visible and UV range, which can in turn ionize the gas atoms or extract electrons from the surrounding electrodes (photoelectric effect), resulting in creation of even more charge.[6] It could even lead to a formation of a new avalanche separated from the primary one. If the fields are strong enough, the process can be self-sustaining, thus resulting in a complete electric breakdown. Suing pure noble gases is not sufficient to prevent this problem. Therefore the second constituent, called quenching gas, has to be added to the gas content. Proper candidates are organic, polyatomic gases like CO_2 or CH_4 with a large photon absorption cross section in the visible and UV range. Adding an extra fraction of quenching gas (like N_2) can lead to even more stable conditions.
Therefore the R&D prototype detector was operated with both Ar-CO_2 and Ne-CO_2-N_2 gases. The ratios of the components in the gas mixture are indicated behind the gas name. Typically for Ar-CO_2 two different ratios are used (90 - 10 or 70 - 30), while Neon is normally contained in the gas mixtures Ne-CO_2 (90 - 10) or Ne-CO_2-N_2 (90 - 10 - 5).[7]

Despite huge efforts to maintain 100% granularity, impurities in the gas are inevitable. In mixtures containing electronegative molecules such as O_2, H_2O or CF_4, electrons can be captured to form negative ions. These electronegative molecules are not desired because they capture primary electrons and thus spoil the energy resolution. However, constantly flushing the detector suppresses the water or oxygen content to few parts per million (ppm) in the detector volume.
While in experiments this basic effect is ubiquitous, in the simulation framework it needs not be taken into account.

[6] This effect is usually called *photon feedback*
[7] in this case normalized to 105%

2.2 Reference simulations with a point-like source

This section is dedicated to a reference simulation with a point like source (i.e. without spatial extension) in order to understand firstly the behavior of the α-particles in the gas volume. Afterwards the ionization of the gas due to the energy loss of the incoming radiation is analyzed.

2.2.1 Energy deposition and Bragg curves

The process of detection in the simulated gaseous detector starts with the emission of charged particles from a radiation source. Here an ideal, point like source is considered which emits alphas with a certain energy fixed by the simulation.
The particles traversing the active volume of the detector interact with the gas molecules. Due to inelastic collisions[8] with the bound electrons of the atoms, the alphas loose their energy or finally can be stopped in the gas. Generally it is quite complicated to calculate the exact energy deposit of the incoming particles, since it depends on the magnitude of the alpha-atom (molecule) scattering cross section (and this in turn is only determinable if the quantum mechanical rotational and vibrational levels of the molecules as well as the drift velocity and diffusion of the alpha are known).
Nevertheless it is possible to calculate the mean energy loss of a charged particle in a certain medium by using the quantum mechanical, relativistic Bethe - Bloch formula [31]:

$$-\langle\frac{dE}{dx}\rangle = 2\pi N_a r_e^2 m_e c^2 \rho \frac{Z}{A}\frac{z^2}{\beta^2}[\ln\frac{2m_e\gamma^2 v^2 W_{max}}{I^2} - 2\beta^2], \tag{2.1}$$

where:

$$\begin{aligned}
\rho &= \text{density of the absorbing material (here the gas mixture)}\\
z &= \text{charge of incident particle in units of e}\\
Z &= \text{atomic number of the absorbing material}\\
A &= \text{atomic weight of the absorbing material}\\
I &= \text{mean excitation potential}\\
W_{max} &= \text{maximum energy transfer in a single collision}
\end{aligned}$$

The formula above is part of G4EmLivermore, the physics list for low-energy electromagnetic interactions, which is used in the simulation.
Now the following situation is simulated: The point like source is placed in the center

[8] Elastic scattering on the nuclei is possible too, but negligible compared to inelastic collisions.

of the PCB hole (see fig. 2.1) and emits α-particles perpendicular into the active volume of the detector. Four simulations are done with four different gas mixtures $ArCO_2$ (70 - 30), $ArCO_2$ (90 - 10), $NeCO_2$ (90 - 10) and $NeCO_2N_2$ (90 - 10 - 5), that are successively set into the volume. In each gas the particle energy of the α's is set to 5.2 MeV, 5.5 MeV and 5.8 MeV.[9]
Then the range, i.e. how far the particles drift till they stop in the gas, and the energy loss per mm are analyzed. The corresponding Bragg curves for each gas and particle energy are illustrated in the diagrams below.

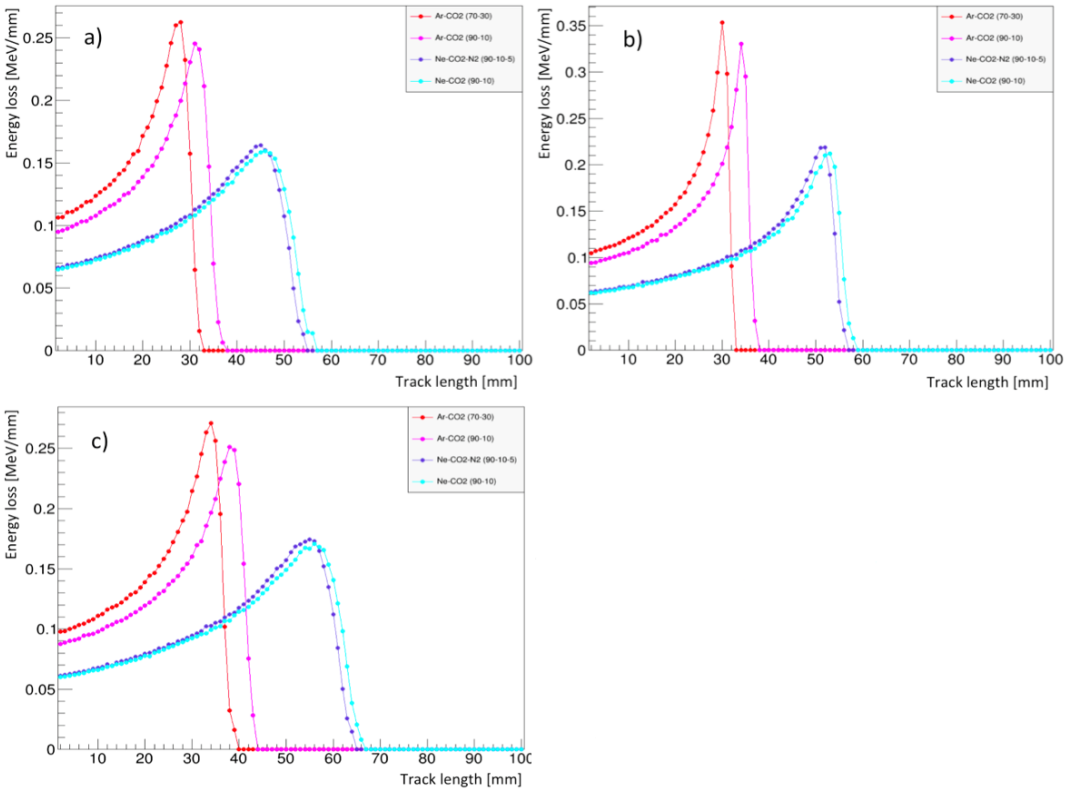

Figure 2.3: GEANT4 simulation of the ranges in different gas mixtures of alpha particles: a) Bragg curves for $E_\alpha = 5.2$ MeV, b) $E_\alpha = 5.5$ MeV, c) $E_\alpha = 5.8$ MeV

By comparing the plots in fig. 2.3 it can be seen, that the higher the energy of the incoming α-particles is the longer is the range in the volume. Also for argon mixtures all curves are, in contrary to the neon based gas, steeper and the track

[9] These energies are chosen because they come close to the radiation energies of ^{239}Pu, ^{241}Am and ^{244}Cm of the real mixed source.

length is almost 40% shorter due to the Z-dependency of the mean energy loss (see eq. 2.1) .
A similarity between the simulated plots and the experimental diagram on page 9 can be noticed: The plots show that the particles with $E_\alpha = 5.8$ MeV (equivalent to the highest energy component of ^{244}Cm and also for the mixed source) have a range of around 50 mm in Ar-CO_2 (90 - 10) and almost 70 mm in Ne-CO_2-N_2 (90 - 10 - 5). At these values the discharge probability for both gas mixtures drops significantly.
Furthermore the Bragg peaks simulated for argon mixtures are higher and narrower, which means that the alphas deposit more energy nearly the range maximum than in the neon mixtures. As a result, locally higher charge densities are achieved, which matches well with the experimental plot in terms of the charge density hypothesis: the discharge probability in argon based gas mixture is higher than in neon based.

2.2.2 Ionisation of the gas and "Bragg cluster" definition

Still not mentioned is the fact, that the Bragg curves totally differ for $NeCO_2$ (90 - 10) and $ArCO_2$ (90 - 10), although the amount of quencher is the same in both mixtures. According to that the mass and atomic number of the noble gas components have to dominate over the range and the steepness of the curves. Since argon has a higher ordinal number than neon, in a gas filled with $ArCO_2$ the probability for an inelastic collision between incoming particle and electrons is increased. Therefore the alpha-particles loose much faster their energy and thus the mean free path is smaller respectively to that of the lighter noble gas.
In order to create an electron - ion pair, the energy deposit must be equal or higher than the effective ionization potential[10] of the gas molecule. The characteristic ionization potentials of the four gas mixtures considered in the simulation are listed in table 2.2.

gas mixture	effective ionization potential W_i [eV]
Ar-CO_2 (70 - 30)	28.10
Ar-CO_2 (90 - 10)	28.77
Ne-CO_2 (90 - 10)	38.10
Ne-CO_2-N_2 (90 - 10 - 5)	37.29

Table 2.2: The in the simulation considered gas mixtures together with each effective ionization potential. [32]

[10] In an effective ionization potential both the excitation and ionization energy are considered.

For example, if an incident alpha-particle deposits 5 MeV in Ar-CO_2 (90 - 10), then the total amount of produced free electrons in average is:

$$\#\ electrons = \frac{\Delta E_\alpha}{W_i} = \frac{5MeV}{28.77eV} = 173.8 \cdot 10^3 \tag{2.2}$$

In GEANT4 the track of the alpha-particles in the drift volume is divided in several steps, where at each step N electrons are created at rest (N is calculated from eq. 2.2). Since these electrons are not equally distributed within a GEANT step but created in one place, they have the same spatial coordinates for each step.
Now applying the same calculation with Ne-CO_2-N_2 as the gas content, the alpha would produce $134.1 \cdot 10^3$ electrons. So at a given gain the charge density in the argon based mixture would be $\frac{173.8}{134.1} = 1.3$ times larger.
As a consequence, the simple calculation together with the experimental observation (see fig. 1.7) explain the strong dependence of the discharge probability on the used gas mixture. But by normalizing the gain and assuming that the charge density hypothesis can be accurate, the spark rate will be dependent of the created electron density, no matter which gas content is chosen (in general however many other factors need to be considered in addition to describe the origin of the electrical discharges). [26]

In the next step a static (i.e. without electric field) simulation is performed in order to get more informations about the amount of electrons that alphas produce at a certain position. The point like source still remains unchanged at the center of the cylindrical hole. But the PCB plate is removed, since no electric field is applied. The source emits $5 \cdot 10^5$ α-particles (from now on often called *events*) isotropically towards the drift volume.[11] Each of the particles has the fixed energy $E_\alpha = 5.2$ MeV and Ne-CO_2-N_2 is the chosen gas mixture in the further simulations.

As already mentioned in the lower section on page 9, in the simulation only one single-GEM layer is implemented into the detector to avoid large diffusion effects of the electrons, that generally occur in multiple GEM based detectors. Furthermore the GEM foil doesn't contain any holes, since no electrical field is set inside the gas box, in order to simplify the simulations. In this chapter namely the charge density of the electrons inside the GEM area to the number of alpha-particles that penetrate it is of interest.

[11] The amount of the events is arbitrary set to that value. The only requirement is, that the number has to be large to get high statistics.

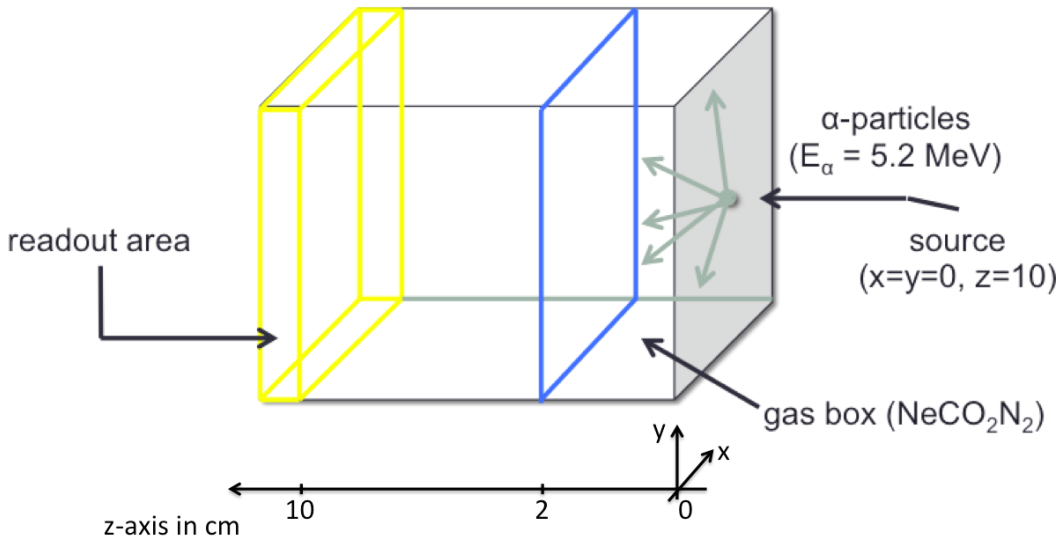

Figure 2.4: Draft of the gas detector together with the point like source.

In fig. 2.4 a simple sketch of both the detector and point like source is drawn. The alphas (indicated by the grey arrows) are emitted isotropically in positive z direction, so that all events interact with the molecules in the gas volume.
The blue area in the figure above indicates a possible position of the GEM layer. From now on the distance d between GEM (the thickness is set to 0.5 mm) and source is adjustable in such a way, that the z-position of the center of mass of the GEM foil is changed from 0 cm to 6 cm in 5 mm steps. At each point the number of the incident particles, that traverse the layer, as well as the amount of created electrons inside the area are counted.

Thus the blue area plays the role of a simplified GEM foil without electric field. Except the thickness (0.5 mm)[12], it has the same dimensions as in the R&D setup (10 cm x 10 cm in length and width).
If the position of the "GEM structure" is set to 10 mm distance from source, then the distribution of the α-particles penetrating the area has the form which is illustrated in fig. 2.5:

[12]In chapter 2.4 the thickness of the GEM foil will be varied in order to look how the electron density inside the area changes for each distance

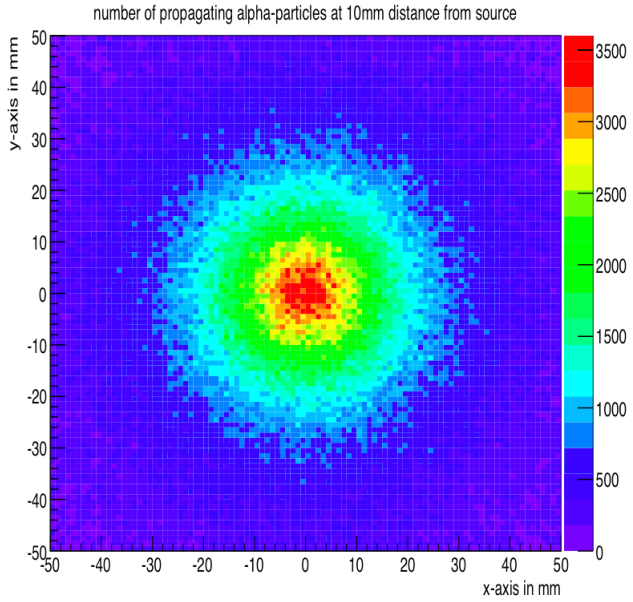

Figure 2.5: 2D plot of the spatial distribution of the α-particles penetrating the area at 10 mm distance from source

On the one hand this two-dimensional diagram shows, that the most alpha-particles hit the center of the readout area due to the bigger solid angle seen from the source. On the other hand the circular shape of the distribution confirms, that indeed the particles are emitted isotropically.

Actually not all particles that were emitted from the point like source hit the GEM area. The diagram on the next page shows the percentage of the detected alphas as a function of the distance between source and readout plane.
What can be seen is that the ratio of the alpha-particles, that penetrate the GEM, to the total number of α's emitted from the mixed source has a linear dependence of the distance between GEM foil and source. The reason for this linearly decreasing curve is a purely geometrical effect:
The further the GEM foil is moved away from the source, the more α-particles can leave the drift volume without hitting the GEM area (assumed that the size of the Gas Electron Multiplier does not change).

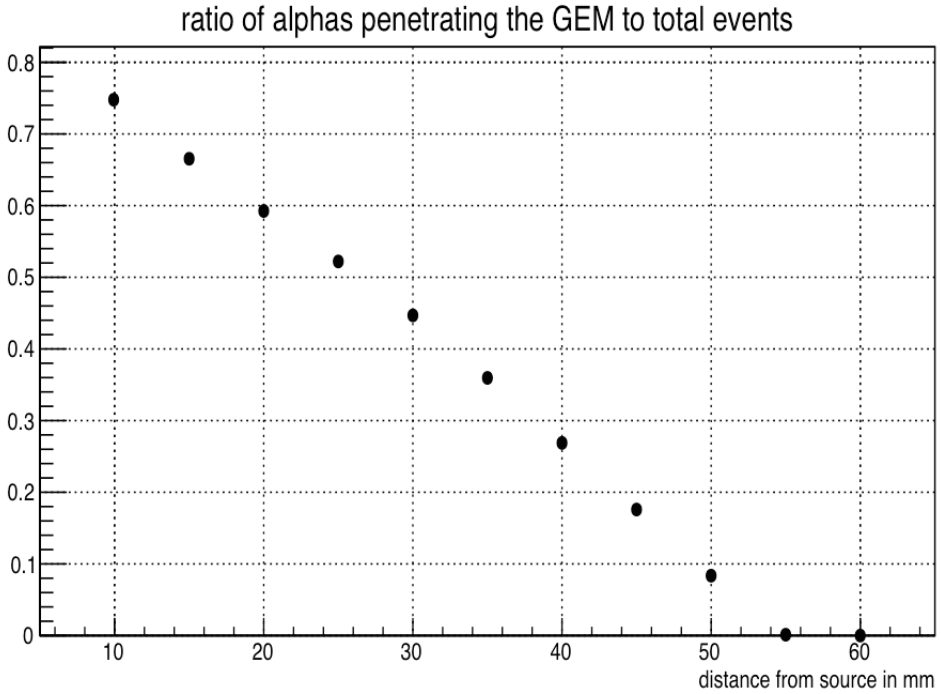

Figure 2.6: Plot of the ratio of α-particles penetrating the GEM area to the primary number of emitted α's. The number of detected particles decreases linearly with the distance.

In that simulation the behavior of the Bragg curve corresponds to the purple curve in fig. 2.3 a), where the maximum track length of $\sim$ 55 mm of the alphas can be read out. The value matches very well with the plot of the ratios.

Due to the absence of an electric field the electrons, that are created by the incoming alpha particles in front of the readout area, are not accelerated to the GEM foil and thus not taken into account when enumerating the total number of created electrons within the area.
Considering now the x - y - distribution of the produced electrons at 10 mm distance from the source, it gives the following picture:

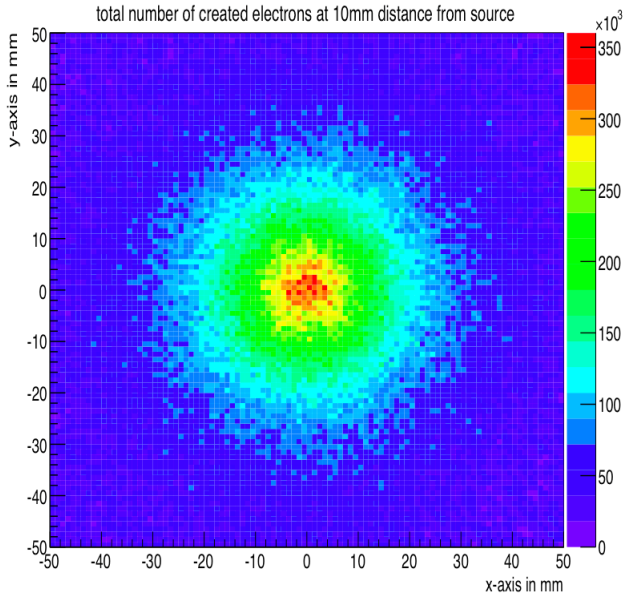

Figure 2.7: 2D plot of the spatial distribution of the created electrons within the GEM structure at 10 mm distance from source.

Precisely because most alpha-particles drift through the center of the area, the highest produced electron density is located at x = y ≈ 0.
In order to normalize the total charge density by the α's traversing the GEM structure, fig. 2.7 is divided by fig. 2.5. The obtained distribution for the created electrons per alpha particle penetrating the GEM area at 10 mm distance is depicted in the figure 2.8.
Therefore the distribution is reversed in comparison to the previous plots 2.5 and 2.7: the counted alpha-particles, i.e. the α's that hit the foil, produce more electrons at the edges of the GEM area as in the center. For example, an α-particle that drifts through x = y = 0 creates approximately 90 electrons within an area of 1 x 1 x 0.5 mm, whereas another alpha produces more than twice electrons (≈ 210) at x = y ≈ 50 mm. That is obvious, since the particles have a longer path till they reach the edges and thus come closer to the Bragg peak.
The same considerations are done for other distances to the source and are illustrated in appendix B fig. B.1. Clearly visible are the red rings, which correspond to the Bragg peak where the most electrons per event are created. Because of the isotropically radiation of the alpha-particles, they form a donut-shape.

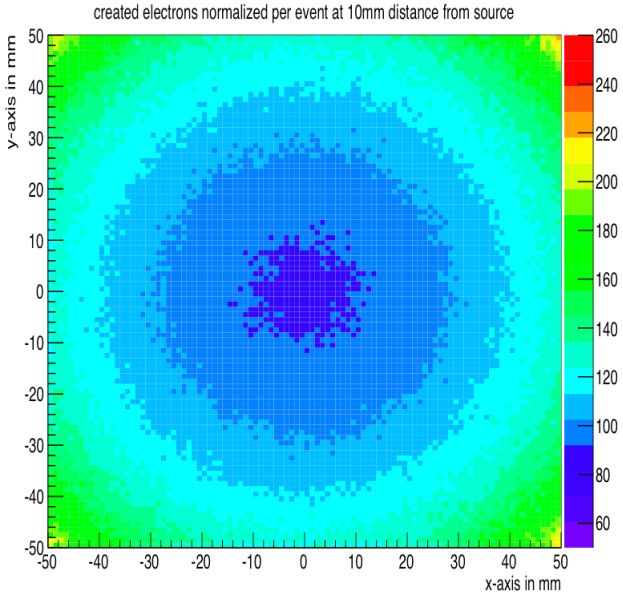

Figure 2.8: 2D plot of the spatial distribution of the created electrons, that are normalized per incoming event, within the GEM structure at 10 mm distance from source.

Fig. 2.9 points out, that the average number of electrons produced by one alpha increases roughly linear up to ~ 45 mm and then drops abruptly within 10 mm from the maximum (~ 190 e^-) down to zero.

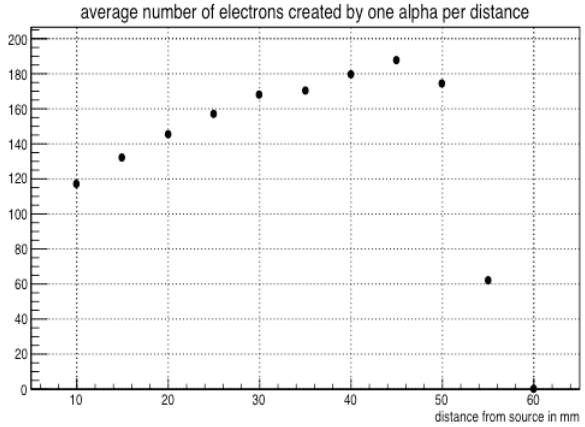

Figure 2.9: Plot of the average number of electrons created by one α-particle as a function of the distance.

Coming back to the graphic representation in fig. B.1, one defines a "Bragg cluster" within the red rings: a region with 1 mm^2 surface, where at least x_{Bragg} electrons per incoming particle are produced. The variable x_{Bragg} can be set to each favored value, but to study high charge densities it is advisable to give x_{Bragg} a huge number.

In the plot below, for different values of x_{Bragg} (between 220 and 250) the amount of the Bragg clusters is counted and afterwards divided by the number of α's hitting the GEM foil.
The results are plotted against the distance to the source.

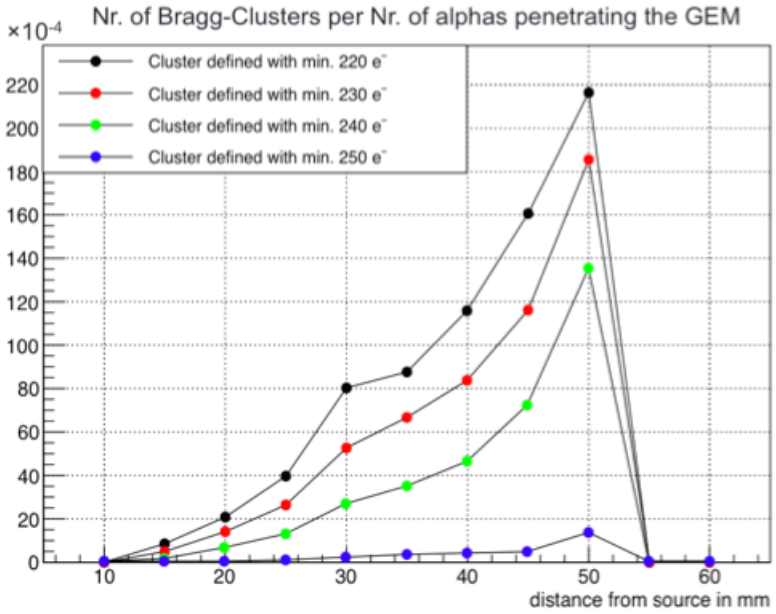

Figure 2.10: Diagram showing the number of Bragg clusters (defined by the amount of the inlying electrons) divided by the amount of α's that penetrate each Bragg cluster region. With bigger distance the values increase until a certain maximum at 50 mm, then they drop to zero.

It can be clearly seen, that all four curves rise with increasing distance and reach a steeply peak at 50 mm.
In other words, the Bragg cluster per se is defined as the cluster with the highest charge density created by one incoming alpha. Dividing the Bragg clusters by the penetrating alpha-particles lead to a quantity that can be compared with the probability to find such a cluster per penetrating particle at a certain distance. For example,

when one alpha hits the GEM at 40 mm distance from source, the probability that it creates more than 220 electrons in a 0.5 mm^3 volume in the GEM is nearly 1.2 %. However, at 50 mm distance the probability is almost twice as high ($\sim$ 2.2%).
Since in the experiment the number of α-particles hitting the readout area can't be counted, but the total number of events emitted from source is known, the amount of Bragg clusters is divided by $0.5 \cdot 10^6$. The result is shown in fig. 2.11.

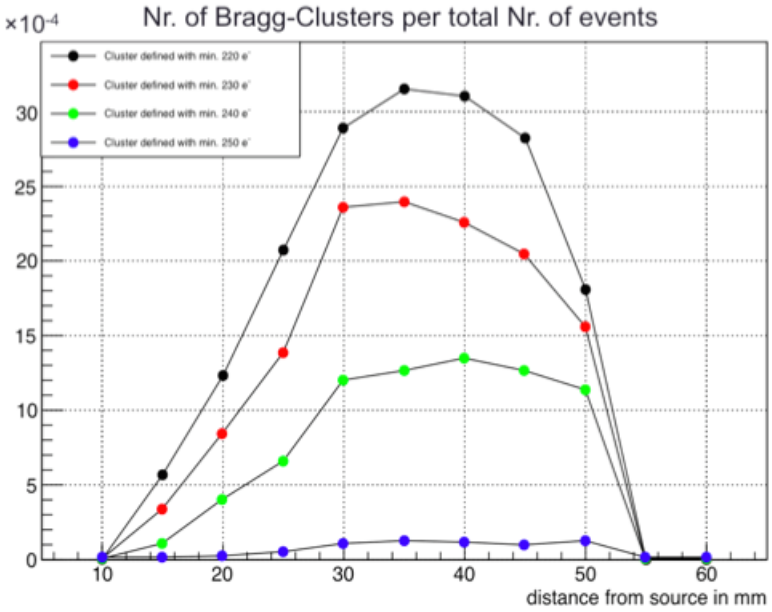

Figure 2.11: The same diagram as in fig. 2.10, except that the Bragg clusters are divided by the total number of events (i.e. $5 \cdot 10^5$). The curves have a broad plateau from $\sim$ 30 mm to $\sim$ 50 mm like in the experimental observation in fig. 1.7.

Also in the diagram above the curves increase up to roughly 30 mm, but followed by a broad plateau of 20 mm length instead of a peak like in fig. 2.10.
Noticeable is the fact that in both plots the number of Bragg clusters with the defined x values is zero in the first 10 mm. That means that the probability to find a charge density of $\frac{min.\ 220e^-}{\#\ penetrating\ \alpha's}$ or a density of $\frac{min.\ 220e^-}{\#\ total\ events}$ per 1 mm^2 is always 0 for a point like source with $E_\alpha = 5.2$ MeV.
Because the events have a max. track length of approximately 55 mm in the gas mixture, logically the curves in both diagrams are constantly zero from 55 mm to 100 mm.

2.3 Simulations with a mixed source

All calculations in the section before are done with a point-like radiation source (no spatial extension) that emits alpha-particles with $E_\alpha = 5.2$ MeV into a Ne-CO_2-N_2 (90 - 10 - 5) gas mixture. Since the experiment is performed with a mixed radionuclide source (see page 10 f.) and the aim is to reproduce the experimental data in fig. 1.6 with the simulation, from now on the point like source is replaced by the mixed source.
Basically the radionuclides ^{239}Pu, ^{241}Am and ^{244}Cm in the source emit α's with the same rate but with different energies and intensities. Arithmetically averaging the energies weighted with the intensities, the mean α-energy of each nuclide is:

$$E_\alpha = 5.147 \text{ MeV for Pu-239}$$
$$E_\alpha = 5.446 \text{ MeV for Am-241}$$
$$E_\alpha = 5.795 \text{ MeV for Cm-244}$$

Instead of implementing the mixed source with its eight energies from table 2.1 in the simulation, the source is defined to emit randomly one of the energies above with the same activity. But before starting to reproduce similar plots like in section 2.2, it has to be proven whether this simplified Monte Carlo simulation gives nevertheless the same right physical predictions.
For the sake of simplicity in the following the Bragg curve of ^{241}Am is considered.[13]

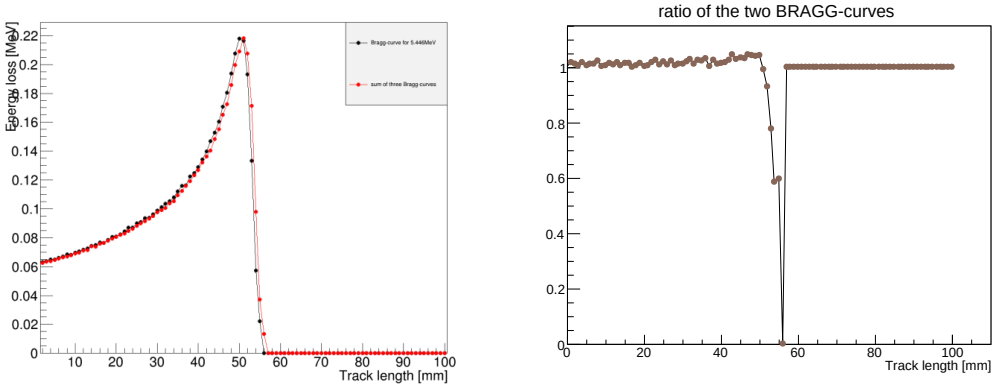

Figure 2.12: a) Left: Comparison between the Bragg curve for $E_\alpha = 5.446$ MeV (black) and the *mean Bragg curve* of Am-241 (red), b) Right: Plot of the ratio of the two Bragg curves.

[13] The calculations are also for both ^{239}Pu and ^{244}Cm valid.

Primarily the energy loss for each alpha-energy (5.388 MeV, 5.443 MeV and 5.486 MeV) is calculated. The corresponding Bragg curves are then weighted with the intensity of each energy and afterwards added in order to obtain the *mean Bragg curve* of the americium nuclide. Analogously the Bragg curve of the average alpha-energy $E_\alpha = 5.446$ of Am-241 is calculated. In order to compare both curves they are plotted in one diagram which is illustrated in fig. 2.12 a). Furthermore both are divided from each other and the corresponding ratio is depicted in fig. 2.12 b).
Now if both Bragg curves were equal, they would describe the same physics of the emitted alpha-particles in the gas volume and the ratio would be constantly one. However, fig. 2.12 b) shows a deviation of the constant at ≈ 55 mm which has nearly the form of a delta peak. This comes from the fact that both curves are shifted by ≈ 1 mm from each other.
Since the height and width are equal, the calculation shows that the deviation is negligible if the charge density is studied only in 5 mm steps. Thus, the simulations are valid when taking the mean alpha-energies of the radionuclides, as long as the steps are not of the order of 1 mm or smaller.

In the real experiment the mixed nuclide source is put within the PCB plate. In order to study possible differences in the results that can occur if a PCB layer is implemented too, the detector is simulated first of all without and afterwards with the PCB plate.
In the figure on the next page the ratios of both independent simulations are plotted against the distance from source (here again the ratio is defined as the number of alpha-particles that penetrate the GEM foil divided by the total number of events emitted from the mixed source).
The black curve for the simulation without PCB layer has approximately the same shape as the curve for the point like source in fig. 2.6, except that the slope is flatter and thus the max. track length is around 10 mm larger due to the higher energy of the radionuclides in the mixed alpha source. Also in this case the shape emerges from the geometrical effect.
In the region between 30 mm and 70 mm the red curve, which represents the result of the simulation with PCB layer, decreases linearly and has almost the same values as for the black curve. However, close to the mixed source (until ~ 25 mm) the values differ totally from the values without plate and do not follow the linear dependence. The flattening of the curve arises in addition to the geometrical cause also from another effect:
While for a detector without a PCB layer all emitted events can penetrate the GEM area (i.e. "can be seen by the GEM") if it is adjusted to an appropriate distance, in the simulation with the PCB plate the particles would stop immediately if they hit the plate. This mechanism is possible since the mixed source is placed on top of the PCB and radiates the alpha particles isotropically into the detector.

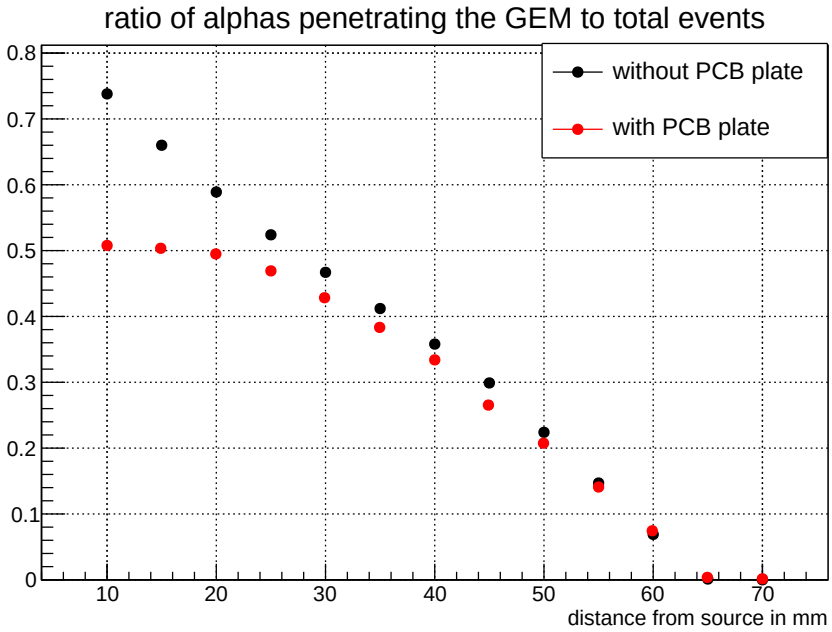

Figure 2.13: Plot of the ratio of α-particles penetrating the GEM area to the primary number of emitted α's. The number of detected particles decreases linearly with the distance for the simulation without PCB (black curve), analogous to fig. 2.6 for the point like source. The red curve is dedicated to the simulation with PCB plate, where a linear drop starts from $\sim$ 25 mm.

Therefore only particles with a momentum direction within the cylindrical hole can drift into the active volume. For example, if the source emits isotropically $50 \cdot 10^3$ α's then only $\sim$ 25 787 particles would arrive the gas box behind the PCB. Thus in the following the total number of events is equivalent to all the α-particles that could be seen by the detector.
In fig. 2.14 left the amount of Bragg clusters normalized per α's penetrating the GEM is shown for the simulation without PCB plate, while in the right plot in fig. 2.14 the same results with PCB layer are depicted. The curves in both diagrams have a similar shape to the results for a point like source simulation (see fig. 2.10). For each x_{Bragg} the probability to find a Bragg cluster per α that penetrates the GEM reaches the maximum at 60 mm.
However, two main differences between the left and right plot are clearly visible: Implementing a PCB plate in the simulation leads to the effect, that the number of Bragg clusters increases by several orders of magnitude. For example, the probability

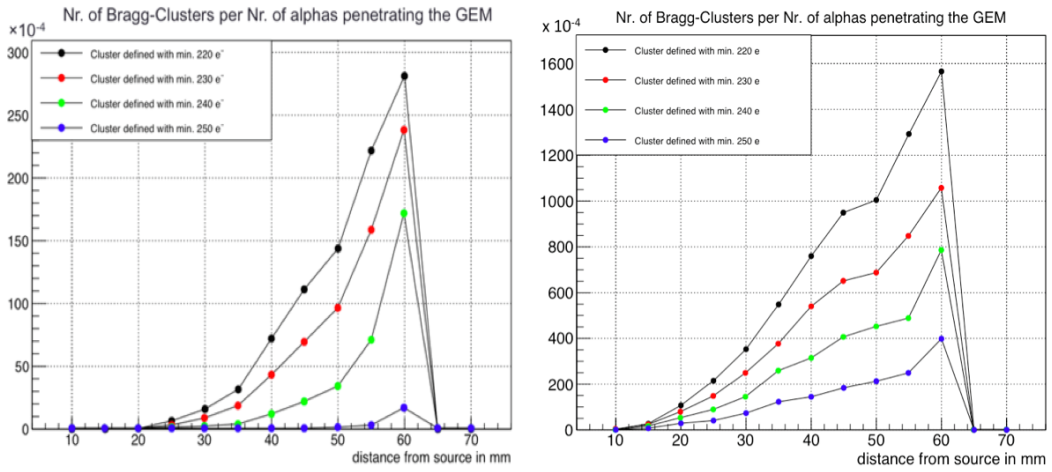

Figure 2.14: Diagrams showing the number of Bragg clusters divided by the amount of α's that penetrate each Bragg cluster region. Left: results without PCB plate, Right: results with PCB plate. With bigger distance the values in both plots increase until a certain maximum at 60 mm, then they drop to zero.

to find a cluster at 60 mm distance is $\sim 2.8\%$, but if a PCB is adjusted in the detector the probability is ~ 15.9 % (for $x_{Bragg} = 220$). That means, that the α's hitting the GEM would produce more electrons within the area. Thus the definition of x_{Bragg} is extended to higher values up to 290 e^-. The plot below shows the amount of Bragg clusters per penetrating α for x_{Bragg} between 260 and 290.

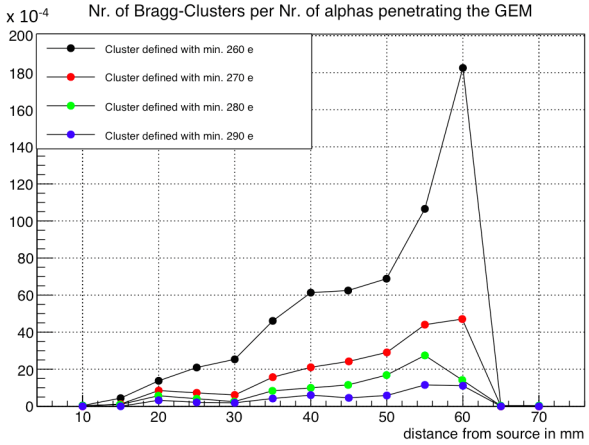

Figure 2.15: Similar plot to fig. 2.14 right, except the different values for x_{Bragg}.

Comparing fig. 2.15 and fig. 2.14 left shows that the values have lie in the same magnitude (up to few percent). The other main difference between the results of the simulation without PCB (fig. 2.14 left) and with PCB layer (fig. 2.14 right and fig. 2.15) is that the latter plots have broader curves.
If the number of Bragg clusters is divided by the total number of events, following diagrams arise as a result:

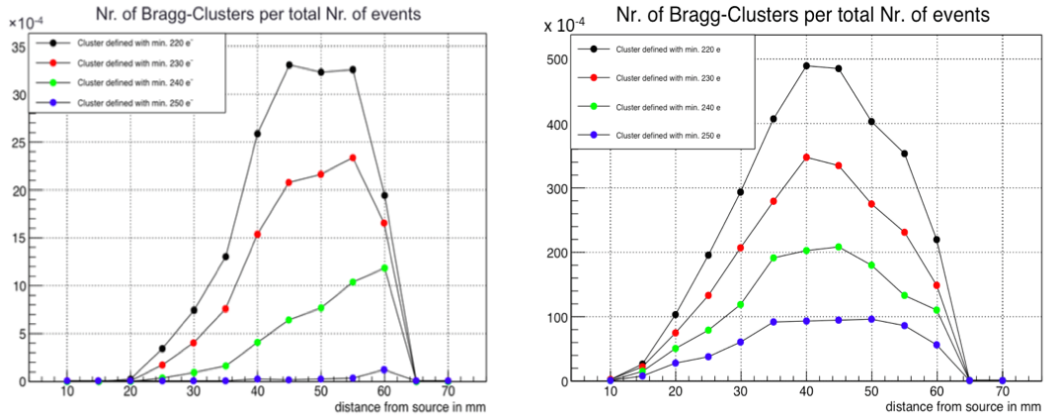

Figure 2.16: Diagrams showing the number of Bragg clusters divided by the total number of events. Left: results without PCB plate, Right: results with PCB plate.

Here the same differences between both simulations appear: the curves are higher and broader if a PCB layer is put in the simulation. Again the following plot gives the results for increased x_{Bragg} up to 290:

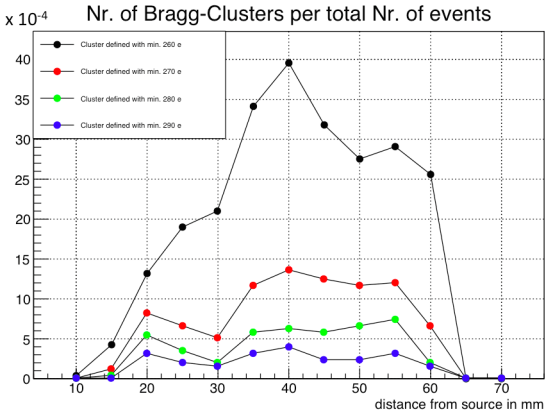

Figure 2.17: Similar plot to fig. 2.14 right, except the different values for x_{Bragg}.

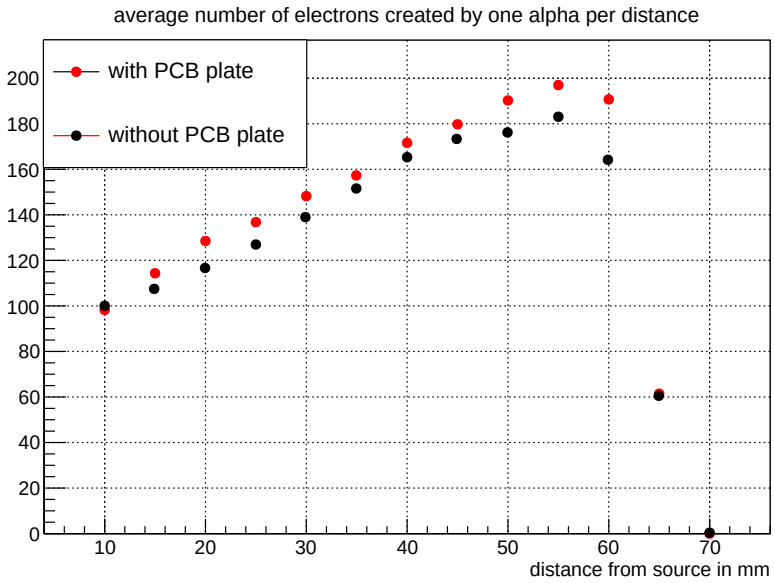

Figure 2.18: Plot of the average number of electrons created by one α-particle as a function of the distance. The red curve (simulation with PCB) has the same shape as the black curve (simulation without PCB) but higher values.

The diagram above points out that at each distance the alpha-particle produces on average between 5 and 10 electrons more if a PCB layer is implemented. Apart from that the curves for both simulations increase linearly up to $\sim$ 55 mm and subsequently drop abruptly to zero.
The reason for the differences between both simulations can be explained with the draft in fig. 2.19 a). If the PCB plate is absent in the simulation, the emitted alphas can loose their energy only due collisions with the gas molecules and thus create electrons which can be detected. This mechanism has been explained in detail in the previous sections. However, if a PCB layer is implemented, three different scenarios can happen:

1. Particles, which drift through the cylindrical hole, are not affected by the PCB plate. Hence no difference in the simulation should appear.
2. Inside the hole the particles can be emitted towards the PCB and finally be stopped there.
3. Particles drift in such a way, that they only brush the outer edge of the layer and thus loose energy but will not be stopped.

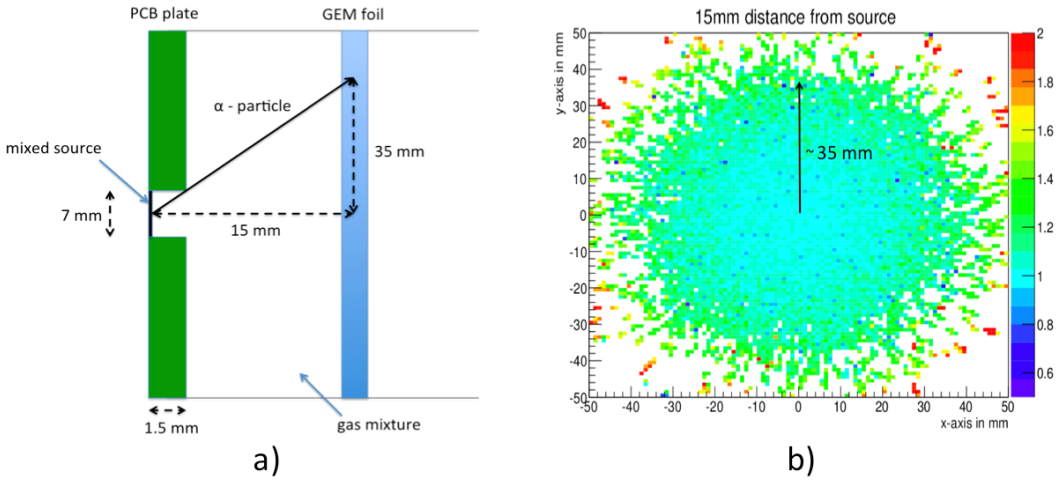

Figure 2.19: a) Sketch of the cross section of PCB plate, mixed source and GEM foil (draft not to scale). The emitted α-particle touches lightly PCB edge and deposits some of its energy. b) 2D-plot showing the ratio of the simulation with PCP layer and simulation if the plate is in absence at 15 mm distance.

In the third case the considered alphas would come closer to the Bragg peak than the not affected alphas from case 1 and thus produce more electrons with smaller distances. For example, if the GEM area is set to 15 mm distance from source and an alpha-particle is emitted from the center of the mixed source in direction towards the edge (see fig. 2.19 a)), then from the *intercept theorem* it follows:

$$\frac{a}{15\ mm} = \frac{3.5\ mm}{1.5\ mm} \Rightarrow a = 35\ mm \tag{2.3}$$

At 35 mm distance from the center of the GEM foil the amount of the produced electrons will be higher if the PCB plate is implemented additionally in the simulation. Like in fig. 2.8 creating 2D plots for the spatial distribution of the produced electrons normalized per alpha penetrating the GEM for both simulation with PCB plate and without PCB plate at 15 mm distance and finally dividing both from each other yields the plot depicted in fig. 2.19 b). The circular area (aqua color) corresponds to the first case where the ratio of produced electrons for each simulation is on average one[14]. Then a continuous transition to the green area takes place (green disc with a radius of $\sim$ 35 mm). The produced electrons within this disc come from the α's that

[14]Not constantly one due to statistical fluctuations in the simulation.

touched the PCB edge. There approximately 1.5 times more electrons are created in comparison to the simulation in absence of the PCB layer. Therefore the plot 2.19 b) confirms very well the validity of fig. 2.15 and 2.17, where the probability of a Bragg cluster defined with min. 290 e^- is not zero.
Up to now a Bragg cluster was defined with the parameter x_{Bragg} as a total number of electrons within a certain area at the GEM foil (1 mm^2). However, one can define x_{Bragg} also as a relative value of the most produced electrons within the region. In other words, e.g. $x_{Bragg} = 5\%$ means that a region with min. 95% of the highest produced electrons is counted as a Bragg cluster. The new definition of x_{Bragg} changes the diagrams in fig. 2.14 and 2.16 and the new plots are depicted in fig. 2.20 and 2.21.

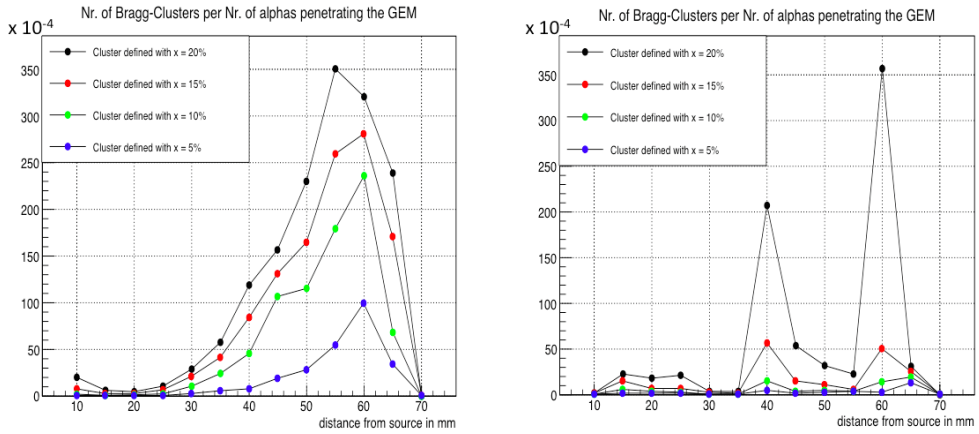

Figure 2.20: Diagrams showing the number of Bragg clusters divided by the amount of α's that penetrate each Bragg cluster region. Left: results without PCB plate, Right: results with PCB plate. x_{Bragg} is defined between 5% and 20 %.

While the shape of the curves for the simulation without PCB plate remain nearly the same like in fig. 2.14 left and 2.16 left between $\sim$ 35 mm and $\sim$ 70 mm, at lower distances however the probability to find a Bragg cluster firstly drops before it starts to increase from 20 mm.
With the new definition of x_{Bragg} the plots in fig. 2.20 right and 2.21 right do not match with the results for the simulation with a PCB plate (see fig. 2.14 right, 2.15, 2.16 right and 2.17). It can be explained as follows: The alpha-particles touched the edge produce in smaller distances more electrons than the other emitted particles and thus produce a high charge density (e.g. 300 electrons in 0.5 mm^3 at 20 mm). Then for example a Bragg cluster is defined when 85 % $\cdot$ 300 = 255 electrons are produced within the certain region. To find such a cluster at 20 mm distance is

extremely unlikely because most alpha-particles don't reach the Bragg peak at 20 mm to produce min. 250 electrons.

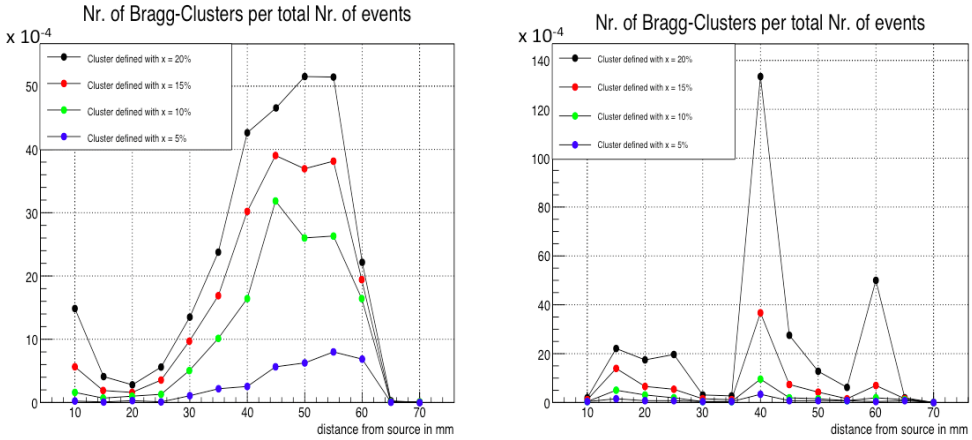

Figure 2.21: Diagrams showing the number of Bragg clusters divided by the total number of events. Left: results without PCB plate, Right: results with PCB plate. x_{Bragg} is defined between 5% and 20 %.

Therefore the right plots in fig. 2.20 and 2.21 represent only the probability of Bragg clusters induced by alpha-particles touched the PCB edge. In order to get the familiar shape of the curves like in the other diagrams, the x_{Bragg}-parameter has to be increased up to 30% or 40%.
The large fluctuations and jumps in fig. 2.15, 2.17, 2.20 right and 2.21 right could be due to statistical nature. To avoid high statistical errors more amount of data is needed, i.e. emitting more events into the active volume of the detector.

In the analysis up to now the GEM thickness was freely chosen, but fixed during the simulation, namely 0.5 mm. Since in reality the GEM foils are much less than 100 μm this value is changed to 0.2 mm[15] and the simulations are done again in order to study possible changes in the results. The new plots are illustrated in the figures on the next page but this time only for the simulation with PCB layer. Furthermore the x_{Bragg}-parameter has been redefined again.
Clearly visible is that the shape and magnitudes of the curves do not change significantly. The width of the broad plateau in fig. 2.23 left and right matches very well with that of the experimental diagram (see fig. 1.7).

[15]If the thickness is set less than 0.2 mm to come as close as in the real experiment, the GEANT4 step length (set to 0.1 mm) has to be smaller.

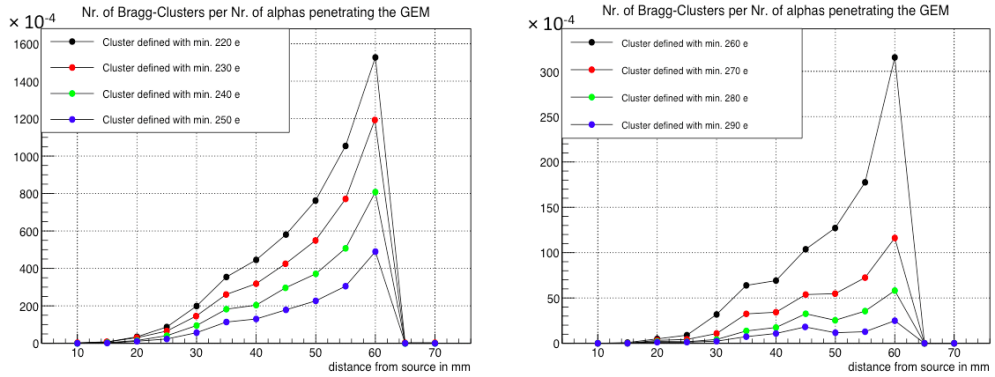

Figure 2.22: Diagram showing the number of Bragg clusters (defined by the amount of the inlying electrons) divided by the amount of α's that penetrate each Bragg cluster region. With bigger distance the values increase until a certain maximum at 60 mm, then they drop to zero. Left: x_{Bragg} defined between 220 and 250 e^-, Right: x_{Bragg} defined between 260 and 290 e^-. The GEM area has a thickness of 0.2 mm.

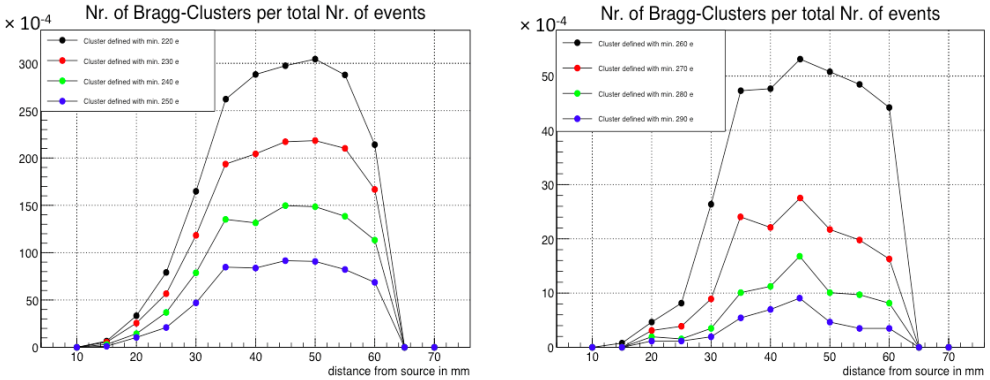

Figure 2.23: Same diagrams as in fig. 2.22, except of that the Bragg clusters are divided by the total Nr. of events (i.e. alpha-particles that could be detected at the GEM foil).

2.4 Simulations with additional el. field

In the previous section a simulation is done in absence of an electric field (static simulation). When a field parallel to the z-axis is applied, the created electrons will be accelerated along the field lines. Since the electrical field is set to 400 V/cm and the GEM foil is implemented without holes (i.e. no strong inhomogeneous field) an electron avalanche is out of question. A state of equilibrium appears immediately between the acceleration and collision with other gas atoms so that the movement of the electrons can be described by

$$z(t) = v_{Drift} \cdot t + z_0 \ , \ x = y = const. \tag{2.4}$$

whereas v_{Drift} is the constant drift velocity for the considered gas medium and z_0 the z-position where the electrons were created. x and y are not affected by the electric field. Besides the straight movement along the z-axis the electrons experience longitudinal and transversal diffusion, which can shift z(t) according Gaussian distribution of width $\sigma_{x,y} = \mathrm{D}_T \cdot \sqrt{\Delta x}$ and $\sigma_z = \mathrm{D}_L \cdot \sqrt{\Delta x}$ (with $\Delta x = v_{Drift} \cdot \mathrm{t}$ and D_T and D_L transversal and longitudinal diffusion coefficients[16]). For the electrical field equal to 400 V/cm the values of these variables are listed in the table below:

Gas mixture	v_{Drift} [cm/μs]	D_L [$\sqrt{cm}$]	D_T [$\sqrt{cm}$]
Ar-CO_2 (70 - 30)	0.931	0.0137	0.0135
Ar-CO_2 (90 - 10)	3.31	0.0262	0.0221
Ne-CO_2 (90 - 10)	2.73	0.0231	0.0208
Ne-CO_2-N_2 (90 - 10 - 5)	2.58	0.0221	0.0209

Table 2.3: Each gas mixture has for fixed electric field = 400 V/cm its typical drift velocity and diffusion coefficients. [32]

In the simulations the max. distance between GEM foil and mixed source is set to 7 cm. This value would correspond to the max. track length of the electrons if they were created close to the source. Due to diffusions in Ne-CO_2-N_2 the track will be shifted by

$$\sigma_{x,y} = D_T \cdot \sqrt{\Delta x} = 0.0209\sqrt{cm} \cdot \sqrt{7cm} \approx 0.55mm \tag{2.5}$$

in the x and y coordinates and by

$$\sigma_z = D_L \cdot \sqrt{\Delta x} = 0.0221\sqrt{cm} \cdot \sqrt{7cm} \approx 0.58mm \tag{2.6}$$

[16] D_T and D_L are proportionality factors between the molar flux due to molecular diffusion and the gradient in the concentration of the species. [32]

in the z coordinate.
The calculations above can be done analogously for the other gas mixtures and the corresponding results will be small too. Therefore it doesn't cast doubt on the validity of the simulations if the diffusion effects are neglected. For larger gas detectors (e.g. range of several meters), however, the diffusion plays an important role for reconstructing the particles track.
In order to study the time distribution of the created electrons in the detector, only one α-particle is emitted perpendicular into the active volume. The electrons are then produced at rest at different distances and drift towards the GEM foil which is adjusted at 70 mm distance from the mixed source. For both gas mixtures Ne-CO_2-N_2 (90 - 10 - 5) and Ar-CO_2 (90 - 10) the results are illustrated in the figure below.

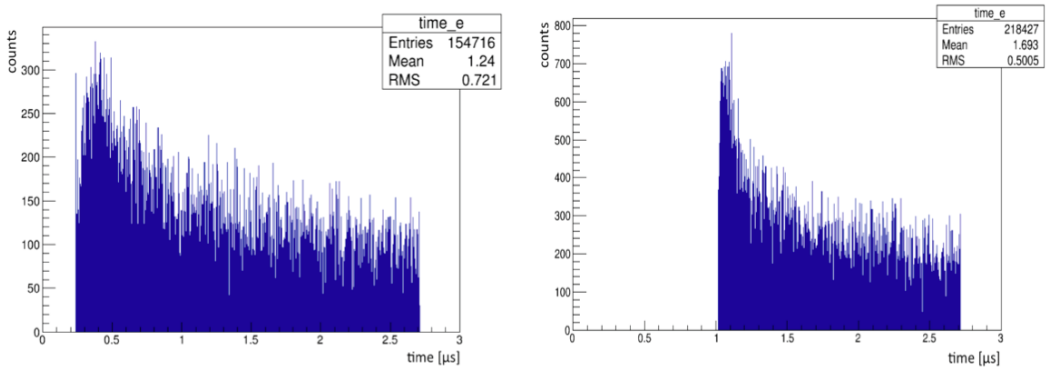

Figure 2.24: Time distribution of the drifting electrons in Ne-CO_2-N_2 (left) and Ar-CO_2 (90 - 10) (right).

Electrons produced at close distance from source have to drift the longest track until they arrive at the GEM foil. Thus the drift time in Ne-CO_2-N_2 is:

$$t = \frac{\Delta x}{v_{Drift}} = \frac{7cm}{2.58\frac{cm}{\mu s}} = 2.71\mu s \tag{2.7}$$

The alpha-particle looses its energy according to the Bragg curve (see fig. 2.3) and consequently produces electrons until it stops $\sim$ 65 mm away from the source. The at the end created electrons therefore have to drift only 5 mm till they were detected by the GEM. The corresponding drift time is:

$$t = \frac{\Delta x}{v_{Drift}} = \frac{0.5cm}{2.58\frac{cm}{\mu s}} \approx 2\mu s \tag{2.8}$$

These calculations are compatible with the plot in fig. 2.24 left. Therefore it is evident, that the time distribution follows an inverse shape of the Bragg curve. The

same calculation can be applied for the Ar-CO_2 case and it can be seen in fig. 2.24 left that the first electrons are detected after $\sim$ 1 μs. Furthermore mentionable is that in the latter gas mixture more electrons are produced in comparison to the neon based mixture due to the higher energy loss of the alpha-particles (see fig. 2.3).
In the next step 10 000 α-particles are emitted isotropically into the detector filled with Ne-CO_2-N_2, mounted PCB plate and applied electrical field in z-direction. In appendix C further time spectra are depicted for the produced electrons as well as for the incoming alphas (the drift time is in the range of nanoseconds due to the high energy of around 5.5 MeV).
The plot below shows the percentage of the detected alpha-particles to the total number of alphas (i.e. 10 000) at several distances from the source for Ne-CO_2-N_2 (90 - 10 - 5) and Ar-CO_2 (90 - 10).

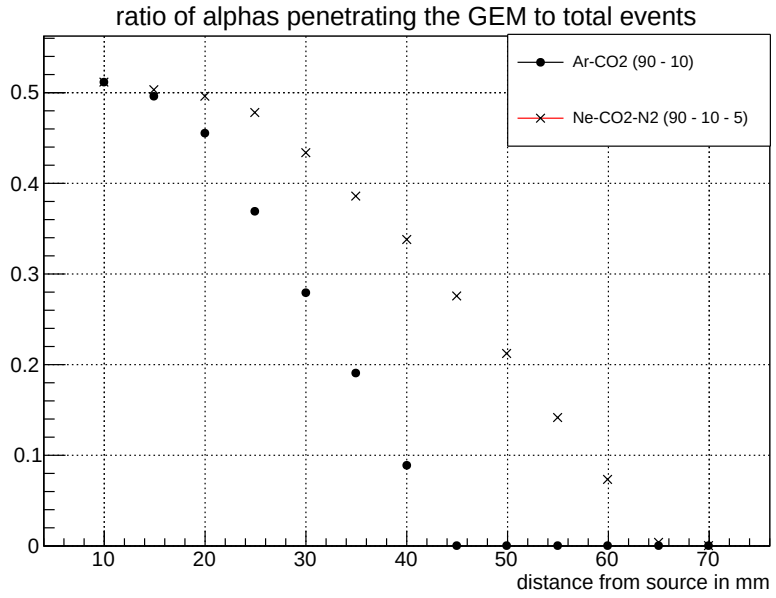

Figure 2.25: Plot of the ratio of α-particles penetrating the GEM area to the primary number of emitted α's. The shape of the curves has already been explained in section 2.3 (see fig. 2.13). All alpha-particles are stopped around 20 mm earlier in Ar-CO_2 (black points).

It can be seen, that the shape of the curves is almost identical with that in fig. 2.13 where a static simulation with implemented PCB layer was performed. As a consequence, the ^{4}He-nucleons are barely affected by the electric field due to the high energy they already have. Furthermore the faster decreasing of the curve for

Ar-CO_2 (90 - 10) confirms the validity of fig. 2.24 right: alpha-particles get stopped much earlier due to the larger energy deposit at smaller distances.
In the following the time is chosen as a parameter (i.e. between 0.5 and 2 μs) and during each time interval the number of detected electrons normalized per total number of alpha-particles is counted. The results are illustrated in fig. 2.26 left. The result of waiting until all electrons are counted (e.g. 3 μs) is shown on the right side of fig. 2.26.

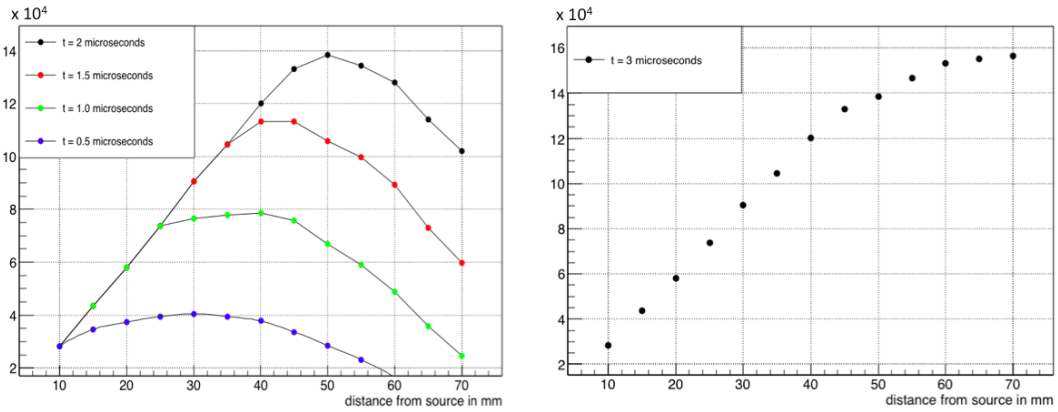

Figure 2.26: Number of electrons divided by the total number of alphas as a function of the GEM distance to the mixed source. Left: results within a fixed time interval. Right: results with no limitation of time (3 μs are enough to detect all created electrons in the active volume).

While the curve in the right plot is strictly monotonically increasing till a saturation value is arrived (around $16 \cdot 10^4$ electrons per incoming alpha-particle), the curves in the left diagram increase up to a maximum (with increasing time interval the maximum shifts towards larger distances) and drop afterwards. The reason for this effect is the following: if the time parameter is set to a small value, then particles produced close to the source can not be counted due to the longer drift time they need until they arrive at the GEM foil.
Especially the green curve for t = 1.0 μs from $\sim$ 25 mm seems to have a similar shape to the blue curve in fig. 1.7 of the experimental data.

Chapter 3

Comparison to the experimental data and outlook

The aim of the bachelor thesis was to connect the discharge probability revealed in the R&D experimental setup shown in fig. 1.7 with the charge density in a single GEM based detector simulated with GEANT4.
After the implementation of the detector with similar size to the experimental prototype detector, the first simulations were done with a point like source without electric field in order to have a reference to the further analysis and to study the behavior of the alpha-particles in the gas volume together with the produced electrons.
Since high electron densities created in a small region in the GEM area could cause an electrical discharge (charge density hypothesis, see section 2.1), Bragg clusters were defined and the probability to find such a cluster per incoming alpha-particle was studied at different GEM distances. The corresponding diagram is illustrated in fig. 2.11. The shape of the curves seem to have a similarity with the experimentally determined blue curve in fig. 1.7. However, at low distances from the source as well as from 55 mm the values are completely different with the observed values from the experiment.
To come closer to the experimental setup, the point like source was replaced by the same mixed source used in the experiment. Simulations were performed in absence of the PCB plate (see fig. 2.16) as well as with the plate implemented (see fig. 2.16). By comparing both plots one can see that the PCB layer increases the Bragg cluster probability and thus the probability to find a high charge density at a certain distance. Furthermore the maxima are shifted around 15 mm towards the mixed source and the plateaus are more broaden too. In contrary to the plot of the point like source, this simulation shows that Bragg clusters can occur at 55 or 60 mm which are conform with the experiment (i.e. the discharge probability at these distances is not zero).
Still the falling edge at around 10 mm can not be explained, but by redefining the Bragg cluster (see section 2.3) the simulation yields the result shown in fig. 2.21 left where a minimum at $\sim$ 20 mm can be seen. Since the PCB plate seems to shift

the Bragg cluster curves between 10 and 15 mm, it could move the minimum to the appropriate position. To verify it, the same plot as in fig. 2.21 right has to be performed but with lower values for x_{Bragg}.
Changing the thickness of the GEM from 0.5 mm to 0.2 mm doesn't change the shape of the other results significantly. Since the experimental data has been taken of a detector with applied electrical field of 400 V/cm, also a dynamic GEANT4 simulation has been performed and the corresponding results were illustrated in fig. 2.26. Setting limitations on the time interval, the curves are bend and form a maximum with a broad plateau as in the previous results with the additional effect that electrons now are also been counted at 70 mm.

In the simulated plots a dependence between the discharge probability and the charge density could be observed. In order to obtain the Bragg cluster shape closer to the curve from the experimental setup, the GEM foil has to be implemented with holes and additional inhomogeneous electric field to increase the gain. A next step could be to improve the plots for the Bragg cluster probability by inserting error bars which give the opportunity to describe the behavior of the experimental results more precisely. Furthermore instead of a single GEM foil a triple GEM stack with same dimensions has to be implemented to come as close as possible to the experimental setup. Then the charge densities in the simulation have to be investigated again to obtain a proper insight into the phenomena of electrical discharges in GEM based detectors.

Appendix A

Principal difference between GEM TPC and wire TPC

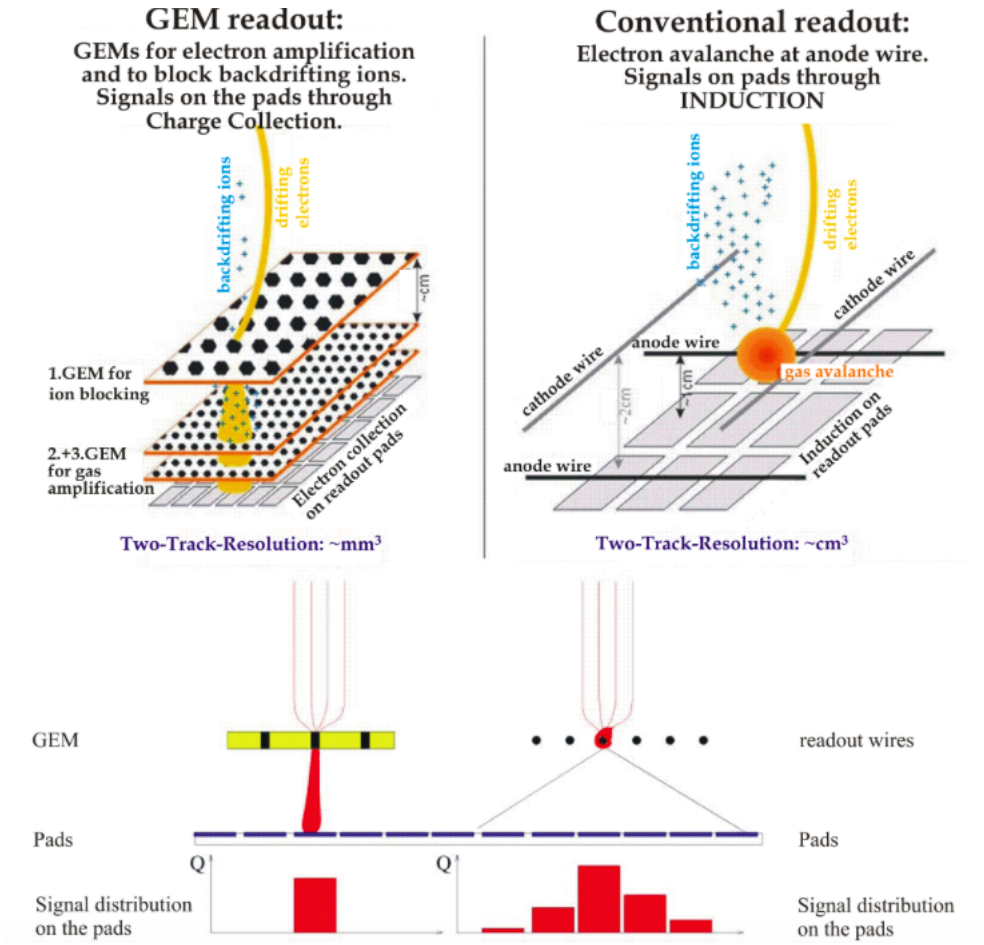

Figure A.1: A major difference between the formed signal in a GEM-TPC (left fig.) and a conventional MWPC-TPC (right fig.): While a wire TPC induces a wide signal on the underlying pads, the signal width of a GEM-TPC is only given by transverse diffusion parameters. These coefficients can be held rather small by applying a magnetic field. [33]

Appendix B

2D simulated plots

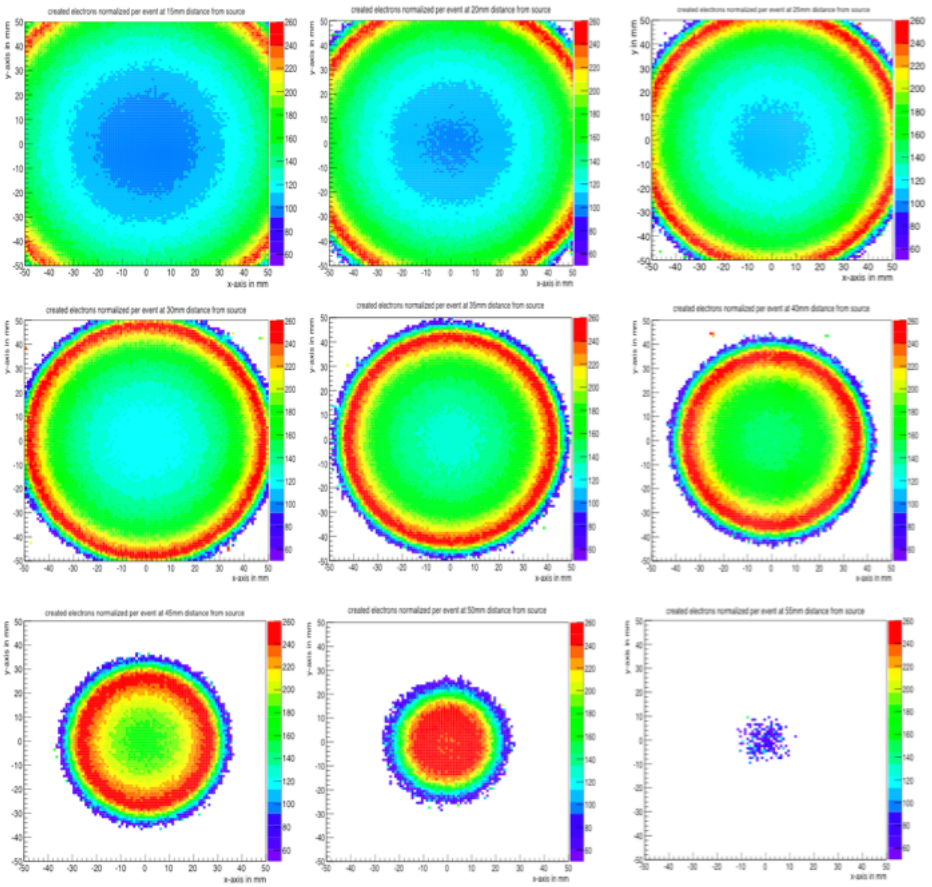

Figure B.1: 2D plot of the spatial distribution of the created electrons, that are normalized per incoming event, within the GEM structure: from top left (10 mm distance from source) to bottom right (55 mm distance) in 5 mm steps.

Appendix C

Time results of the analysis with el. field

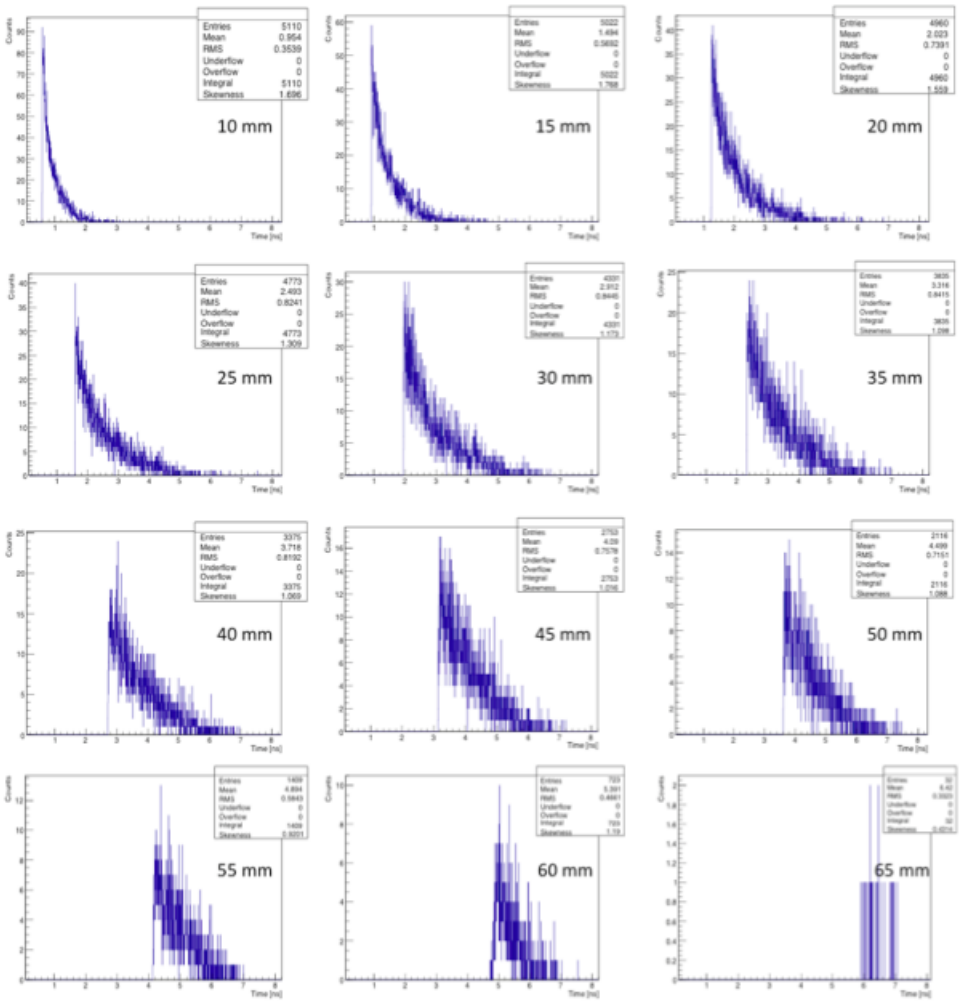

Figure C.1: Time spectra for the alpha-particles in Ne-CO_2-N_2 (90 - 10 - 5)

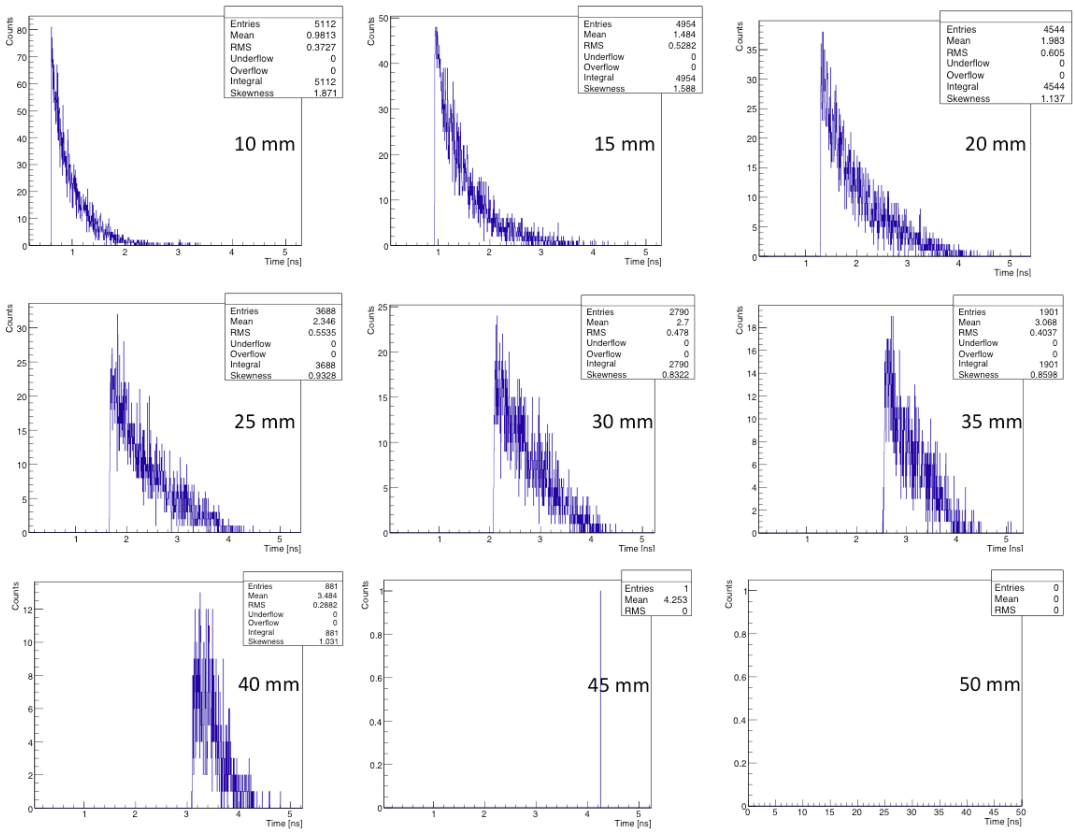

Figure C.2: Time spectra for the alpha-particles in Ar-CO_2 (90 - 10). Time scale in ns.

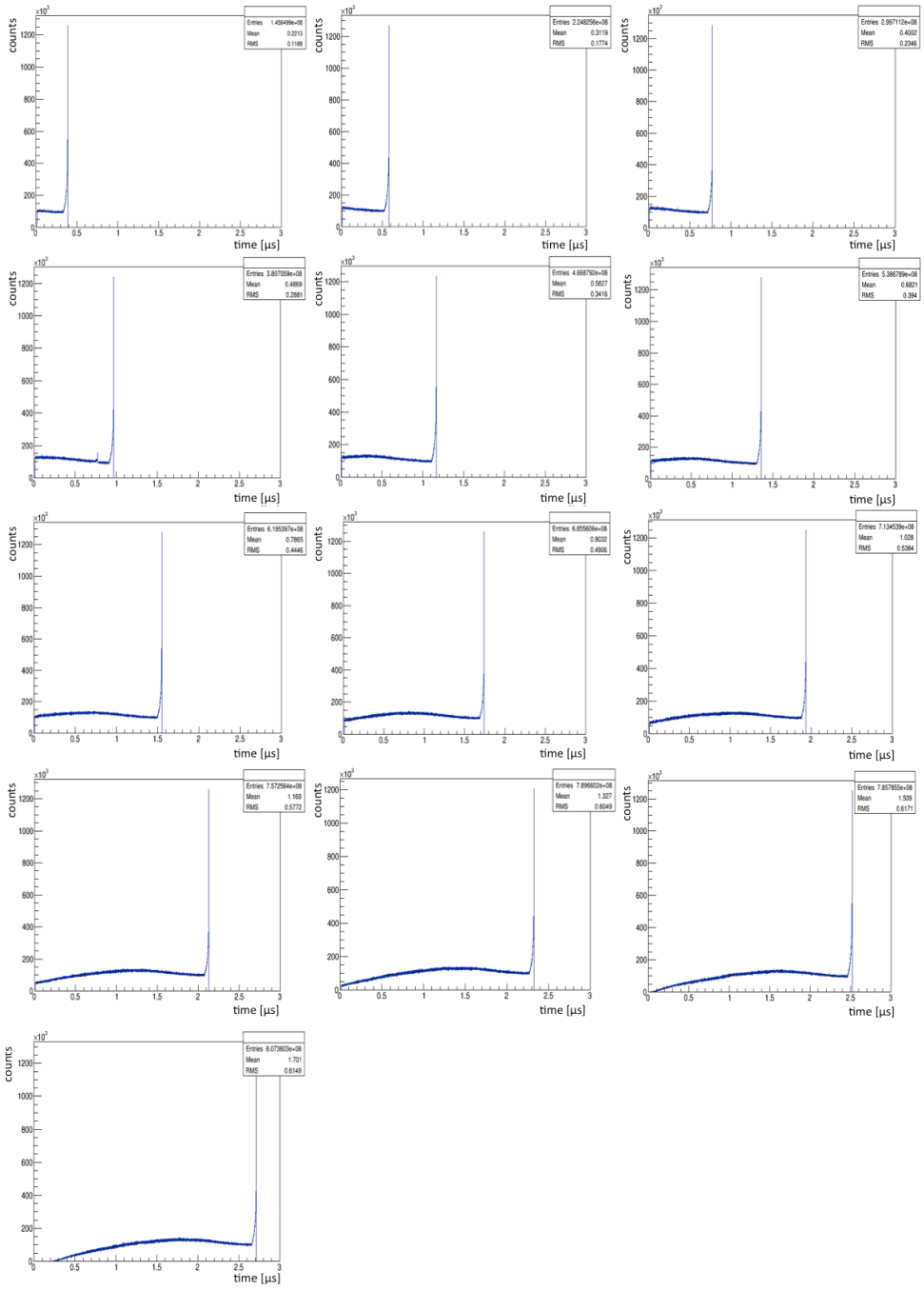

Figure C.3: Time spectra for the created electrons in Ne-CO_2-N_2 (90 - 10 - 5). Time scale in μs.

Bibliography

[1] P. N. Murgatroyd. *Theory of space-charge-limited current enhanced by Frenkel effect*. Vol. Volume 3. 1970.

[2] ALICE Collaboration. *Nucl. Instr. and Meth.* 316 A 622. 2010.

[3] L. Cifarelli. *The Quark-Gluon Plasma, a nearly perfect fluid.* Europhys. News, 2012.

[4] ALICE Collaboration. 5. September 2015. URL: `http://aliceinfo.cern.ch/Public/en/Chapter2/Chap2_HLT.html`.

[5] ALICE Collaboration. *Journal of Instrumentation 3*. S08002, 2008.

[6] M. Ball; F.V. Bohmer; S. Dorheim; C. Hoppner; B. Ketzer. *Technical Design Study for the PANDA Time Projection Chamber.* 2012.

[7] K. Aamodt; A. Abrahantes Quintina; R. Achenbach. *The ALICE experiment at the CERN LHC*. Journal of Instrumentation 3, 2008.

[8] C. Garabatos. *Nucl. Instr. and Meth. A 535, 197*. 2004.

[9] W. Blum; W. Riegler; L. Rolandi. *Particle Detection with Drift Chambers.* Springer-Verlag, 2008.

[10] ALICE@CERN. 5. September 2015. URL: `http://aliceinfo.cern.ch/TPC/node/8`.

[11] G. Knoll. *Radiation Detection and Measurement. 2nd ed.* New York: Wiley, 1989.

[12] KIP Uni-Heidelberg. 6. September 2015. URL: `http://www.kip.uni-heidelberg.de/~coulon/Lectures/DetectorsSoSe10/Free_PDFs/Lecture8.pdf`.

[13] Z. Qiushi; Y. Kun; L. Yanye. *Progress in the Development of CdZnTe Unipolar Detectors for Different Anode Geometries and Data Corrections.* Sensors 2013, 13(2), 2447-2474, 2013.

[14] N. Marx; R. Nygren. *TheTimeProjectionChamber*. Phys.Today 31N10, 1978.

[15] H.J. Hilke. *Time projection chambers.* Rep. Prog. Phys., 73:116201, 2010.

[16] M. Titov. *Gaseous Detectors: recent developments and applications.* arXiv: 1008.3736 [physics.ins-det], 2010.

[17] A. Oed. Nucl. Instrum. Methods A 490, 223, 2002.

[18] C. Altunbas. *Nucl. Instr. and Meth. A 490*. 2002.

[19] F. Sauli. *Nucl. Instrum. Methods*. A 386 . 531, 1997.

[20] B. Azmoun; W. Anderson; D. Crary; J. Durham; T. Hemmick; *A Study of Gain Stability and Charging Effects in GEM Foils*. IEEE Nuclear Science Symposium Conference Record, 2006.

[21] S. Bachmann. *Nucl. Instrum. Methods A 479*. 2002.

[22] C.H. Hahn; I. Kim; W. Kim; J. Yu. *Apparatus for digital imaging photodetector using gas electron multiplier*. 2010.

[23] S. Blatt. *Nucl. Phys. B (Proc. Suppl.) 150*. 2006.

[24] Yu. Ivanuouchenkov. *Nucl. Instr. and Meth. A 422*. 300, 1999.

[25] H. Raether. *Electron avalanches and breakdown in gases*. Butterworths, 1964.

[26] S. Procureur; J. Ball; P. Konczykowski; B. Moreno; H. Moutarde; F. Sabatie. *A Geant4-based study on the origin of the sparks in a Micromegas detector and estimate of the spark probability with hadron beams*. Nuclear Instruments and Methods in Physics Research A 621 177–183, 2010.

[27] ALICE Collaboration. *Addendum to the Technical Design Report for the Upgrade of the ALICE Time Projection Chamber*. ALICE-TDR-016-ADD-1, 2015.

[28] Geant4 Collaboration. *Geant4 User's Guide for Application Developers*. 2009.

[29] UMI. *Studies on Irradiation Effects of Silicon-on-sapphire Devices*. ProQuest LLC, 2008.

[30] Eckert Ziegler. *Calibration Standards and Instruments*. RD1, 2009.

[31] H. Bethe. *Annalen der Physik*. 397, 325, 1930.

[32] ALICE Collaboration. *Technical Design report for the Upgrade of the ALICE Time Projection Chamber*. ALICE-TDR-016. CERN-LHCC-2013-020, 2014.

[33] *A Time Projection Chamber with Gas Electron Multipliers for the TESLA Detector*. 8. September 2015. URL: `http://www-ekp.physik.uni-karlsruhe.de/~ilctpc/GEM-TPC/triplegem.gif`.

Acknowledgements

First of all I want to thank Prof. Laura Fabbietti to make this thesis possible. I am deeply grateful for her guidance, encouragement and patience over the last few months. Thank you so much for your outstanding knowledge in experimental physics, for looking at my work in different ways and for opening my mind.
I would like to express the deepest appreciation to Dr. Piotr Gasik for helping me in any situation and taking time to talk with me on many occasions. I would like to thank him for providing indispensable advice, information and support on different aspects of my project. It was a pleasure for me to take part in his lecture *gaseous detectors* and to learn the physics behind my work.
Also I would like to offer my special thank to Tobias Kunz for his incredible help with software problems of any kind, for his awesome support and the very fruitful discussions we had. I appreciate the feedback and support offered by Dr. Robert Münzer and want to thank him also for teaching me a lot in the lecture *gaseous detectors*.
Of course I want to thank the people I love, my parents and my siblings for their outstanding motivating words and great support. At last I want to thank Jennifer Padberg for her awesome support even though she was also busy with her own bachelor thesis.